Chapter 4

Combined effect of surface polarization and external electrical stimulation towards accelerated osteogenic response of $Na_xK_{1-x}NbO_3$ (x = 02 – 0.8) piezo-bioceramics

This chapter elaborates the results of the combined effect of electrostatic surface charge, dynamic pulsed electrical stimulation and compositional modification towards accelerating osteogenic response of NKN by considering HA as control. The effect of compositional variation in NKN on its structural parameters was analyzed using Rietveld refinement and X-ray peak profile analyses. Further, the mechanical properties were examined. Inductively coupled plasma-atomic emission spectroscopy (ICP-AES) was performed to understand the leaching behavior of NKN in simulated body fluid (SBF). The charges, stored in NKN samples by polarization (@ 25 kV) treatment were quantified using thermally stimulated depolarized current (TSDC) measurement. Further, the effect of polarization on the surface chemistry and wettability was examined using X-ray photoelectron spectroscopy (XPS) and contact angle measurement, respectively. The influence of surface charge on early-stage cell adhesion was studied. Thereafter, the synergistic effect of electrostatic surface polarization charge and dynamic electrical stimulation alongwith compositional modification on cell proliferation, adhesion and differentiation were analyzed. To understand the mechanism of electrostatic/dynamic pulsed electrical stimulation induced cellular response through the activation of signaling pathways, the concentrations of intracellular Ca^{2+} were measured for the non-treated and treated samples.

4.1. Phase evolution

4.1.1. XRD analysis

X-ray diffraction (XRD) analyses of sintered sodium potassium niobate [$Na_xK_{1-x}NbO_3$ (x = 0.2 - 0.8), NKN] and HA samples are represented in Fig. 4.1 (a). The XRD spectra for sintered NKN samples demonstrate the monoclinic structure with space group P1m1 [JCPDS # 77-0038]. In addition, the major peaks of HA are allocated to the single phase hexagonal structure of HA (JCPDS # 09-0432).

XRD patterns were analyzed using Rietveld refinement technique to investigate the structural changes in $Na_xK_{1-x}NbO_3$ after compositional (x) variation. All the refinements for $Na_xK_{1-x}NbO_3$ samples were made on the basis of reference monoclinic $Na_{0.35}K_{0.65}NbO_3$ (JCPDS # 77-0038). Pseudo-Voigt function was used for peak profile refinement. The unit cell parameters for the sintered $Na_xK_{(1-x)}NbO_3$ (x = 0.2 - 0.8) samples were obtained at room temperature using Rietveld refinement. The values of unit cell parameters are mentioned in table 4.1. The values of a, b, c parameters confirm the formation of monoclinic structure of sodium potassium niobates in each composition. The values of lattice parameters for $Na_{0.5}K_{0.5}NbO_3$ are comparatively lower than $Na_{0.2}K_{0.8}NbO_3$. In addition, the position of the most intense diffraction peaks are almost similar for $Na_{0.2}K_{0.8}NbO_3$ and $Na_{0.8}K_{0.2}NbO_3$ however, it shifts towards higher diffraction angle value for $Na_{0.5}K_{0.5}NbO_3$ [Fig. 4.1 (b)]. It may be due to the comparatively larger size (ionic radii) of potassium than sodium in the composition of NKN having equal content of both elements [1, 2].

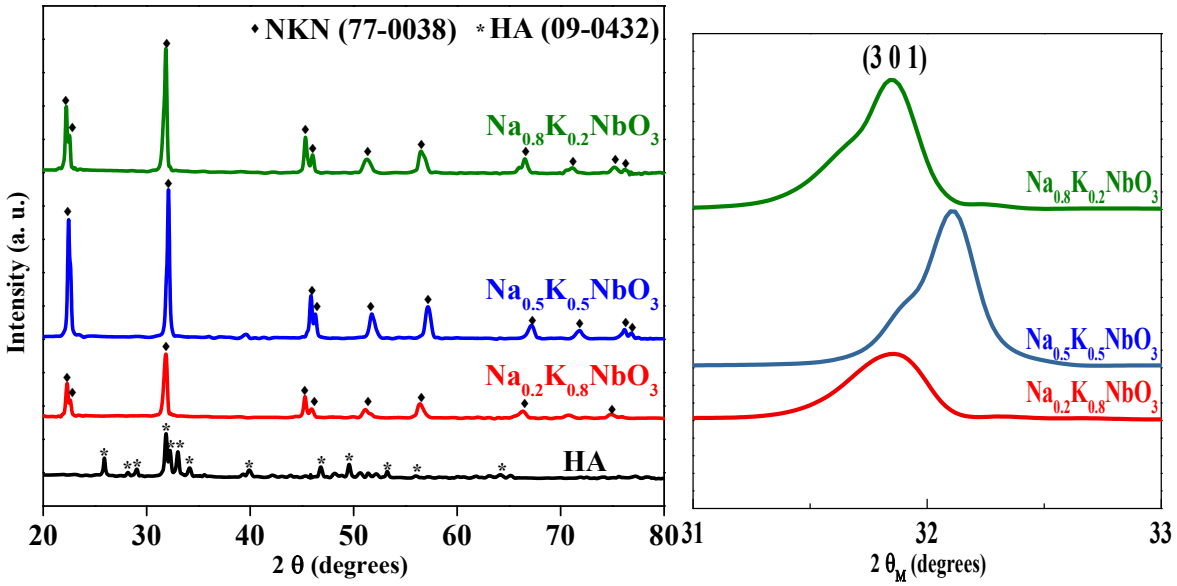

(a) *(b)*

Fig. 4.1. XRD patterns of the sintered HA and $Na_xK_{1-x}NbO_3$ (x = 0.2, 0.5 and 0.8) samples, (b) Positions of the most intense diffraction peaks (2 θ_M) in $Na_xK_{1-x}NbO_3$ (x = 0.2, 0.5 and 0.8).

Table 4.1. The refined unit cell parameters and the positions of most intense diffraction peak ($2\theta_M$) for the $Na_xK_{1-x}NbO_3$ (x = 0.2, 0.5 and 0.8) samples.

Samples	Lattice parameters					$2\theta_M$ (degrees)
	a (Å)	b (Å)	c (Å)	Cell Volume $(Å)^3$	β (°)	
$Na_{0.2}K_{0.8}NbO_3$	9.045	9.119	8.017	661.278	90.367	31.86
$Na_{0.5}K_{0.5}NbO_3$	8.852	9.061	7.794	625.134	90.598	32.10
$Na_{0.8}K_{0.2}NbO_3$	8.942	9.067	7.978	646.744	91.091	31.84

The X-ray diffraction data were plotted in conjunction with Rietveld refinement fitting [Fig. 4.2]. It indicates that the refined patterns are in well agreement with the observed patterns. The finally obtained values of refined parameters such as profile factor (R_p), expected weighted profile factor (R_{exp}), weighted profile factor (R_{wp}), and Bragg's factor (R) are listed

in Table 4.2. The values of goodness of fitting (GOF) for $Na_xK_{1-x}NbO_3$ (x = 0.2, 0.5, 0.8) are 1.10, 1.05 and 1.02, which reflects an agreement between the theoretical and experimental data. In addition, the values of R_p, R_{wp} and R_{exp} further indicate good refinement.

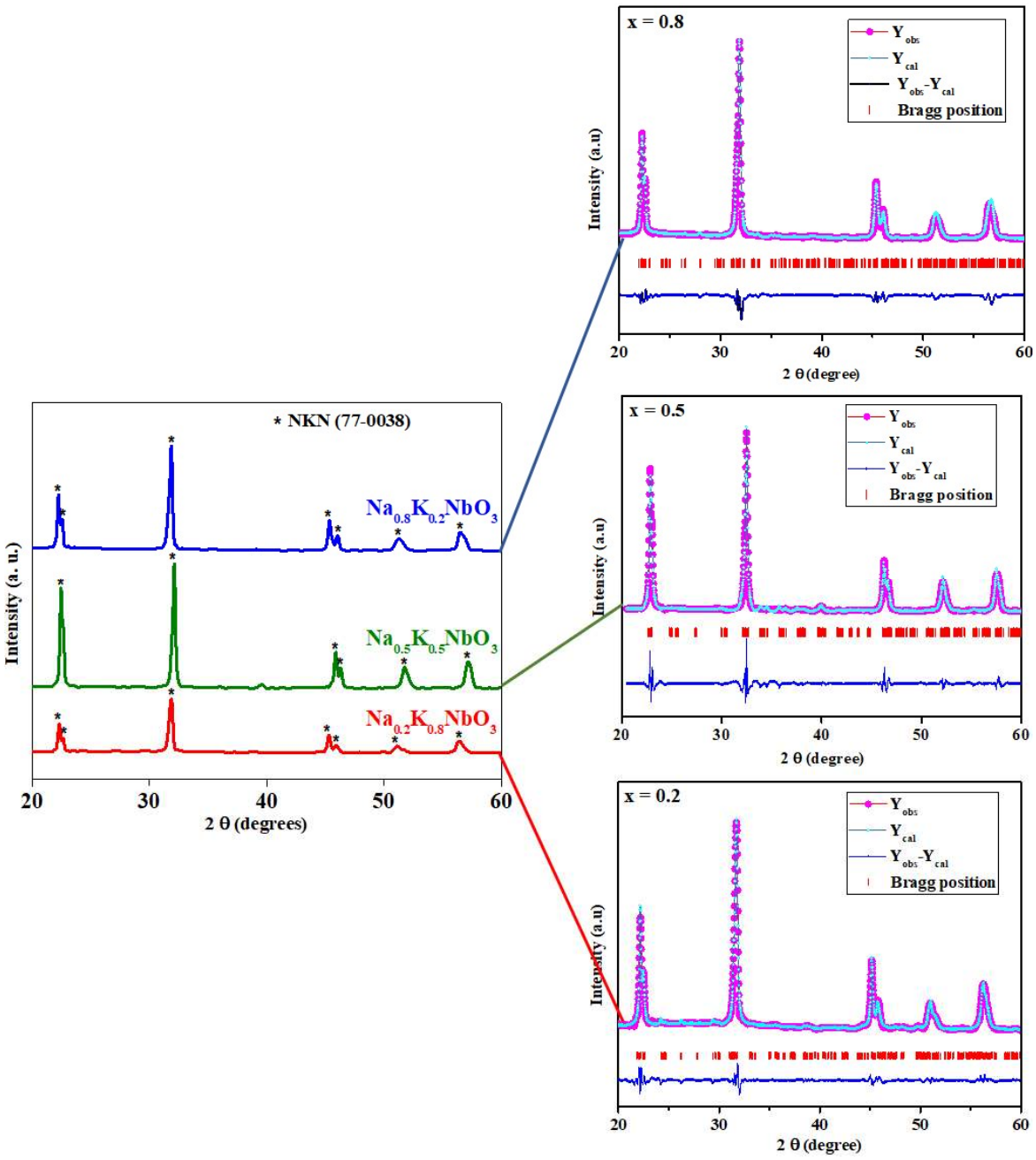

Fig. 4.2. Rietveld refinement analyses for NKN samples. The combined X-ray diffraction spectra for sintered $Na_xK_{1-x}NbO_3$ (x = 0.2 - 0.8) samples. Enlarged view demonstrating the observed and refined data for x = 0.2, 0.5 and 0.8 are illustrated.

Table 4.2. The final obtained values of various refined parameters, corresponding to monoclinic phases in $Na_xK_{1-x}NbO_3$ (x = 0.2, 0.5, 0.8) samples, sintered at 1010, 1075 and 1120 °C, respectively.

	$Na_xK_{1-x}NbO_3$		
	$Na_{0.2}K_{0.8}NbO_3$	$Na_{0.5}K_{0.5}NbO_3$	$Na_{0.8}K_{0.2}NbO_3$
χ^2	1.21	1.09	1.07
R_p	25.8	13.0	16.2
R_{wp}	28.3	14.8	17.4
R_{exp}	25.7	14.1	17
R_f	6.9	7.15	6.5
GOF	1.10	1.05	1.02

4.1.2. Crystallite size and strain measurement

From the diffraction data [Fig. 4.1], the crystallite size and strain have been calculated using Scherrer, modified Scherrer, Williamson-Hall plot, size-strain plot methods. The crystallite size has been obtained using Scherrer formula (Eqn. 3.4) for $Na_xK_{1-x}NbO_3$ ceramic samples [Table 4.3] as.

The modified Scherrer method consider each peak during the measurement of crystallite size and therefore, reduced the error in measurements.

From Eqn. 3.5, by plotting a graph between ln (1/cos θ) along x-axis and ln (β) along y-axis, the crystallite size can be calculated from the intercept (ln $k\lambda/D$) [Fig. 4.3 (a)].

Due to deduction of errors, the obtained value of crystallite size from modified Scherrer method was higher than the value, measured using Scherrer method (Table 4.3).

Williamson Hall plot is an integral breadth method which consider peak width as a function of diffraction angle (2θ) [3]. Apart from the size of crystallites, XRD pattern is also

influenced by the lattice strain. This model assumes NKN material as isotropic and the strain distribution is uniform in all the directions. It clearly demonstrates the size and strain induced deformation with considerable peak broadening. Therefore, total peak broadening will be the sum of size and strain induced broadening of peaks [4].

From Eqn. 3.7, the intercept ($k\lambda/D$) and slope provide the crystallite size (D) and strain (ε) for $Na_xK_{1-x}NbO_3$ ceramic samples [Fig. 4.3 (b)].

Size-strain plot method is more accurate as it preferentially considers the low angle values of XRD reflection peaks where, the XRD data are more accurate and precise than those of the high angle values [5, 6]. In this method, Lorentz and Gaussian functions illustrate the profiles of crystallite size and strain, respectively [5, 6, 7].

From Eqn. 3.8, the intercept $[(\varepsilon/2)^2]$ and slope ($k\lambda/D$) can be used to calculate the crystallite size and strain for $Na_xK_{1-x}NbO_3$ samples, respectively [Fig. 4.3 (c)].

The results of crystallite sizes and/or lattice strain for $Na_xK_{1-x}NbO_3$ (x = 0.2, 0.5, 0.8) samples, obtained from different methods are summarized in Table 4.3.

Among various methods, size-strain plot method provides more accurate data of crystallite size and lattice strain than Williamson-Hall plot, Scherrer and modified Scherrer methods as the high intensity points lie more closure to the linear fit. The Bragg's angle of the most intense peaks shifted towards the higher angle values from $Na_{0.2}K_{0.8}NbO_3$ to $Na_{0.5}K_{0.5}NbO_3$, which may be due to the larger crystallite size of $Na_{0.5}K_{0.5}NbO_3$ sample. However, X-ray peak profile analyses, using different methods, are revealing comparatively smaller crystallite size of $Na_{0.8}K_{0.2}NbO_3$ than $Na_{0.5}K_{0.5}NbO_3$. From $Na_{0.5}K_{0.5}NbO_3$ to $Na_{0.8}K_{0.2}NbO_3$, the potassium (ionic radii: 0.164 nm) content decreases which have comparatively larger ionic

radius than sodium (ionic radii: 0.139 nm) [1, 2]. It may be the reason for smaller crystallite size of $Na_{0.8}K_{0.2}NbO_3$ than $Na_{0.5}K_{0.5}NbO_3$.

Among three compositions of $Na_xK_{1-x}NbO_3$ (x = 0.2, 0.5 and 0.8), Williamson-Hall methods demonstrated comparatively higher value of lattice strain for $Na_{0.5}K_{0.5}NbO_3$ than $Na_{0.2}K_{0.8}NbO_3$ and $Na_{0.8}K_{0.2}NbO_3$ samples [Table 4.3]. Similarly, size-strain plot method is also revealing higher value of lattice strain for $Na_{0.5}K_{0.5}NbO_3$ sample than $Na_{0.2}K_{0.8}NbO_3$. However, the size-strain plot method is demonstrating negative intercept for $Na_{0.8}K_{0.2}NbO_3$ sample and therefore, the measurement of lattice strain is not possible in this case [8]. The higher value of lattice strain for $Na_{0.5}K_{0.5}NbO_3$ may be due to the presence of lattice distortion, dislocations, oxygen deficiency or sintering stress [9, 10, 11]. In addition, lattice strain may also occur due to the lattice contraction or expansion [12].

Table 4.3. Geometrical parameters of solid state synthesized $Na_xK_{1-x}NbO_3$ (x = 0.2, 0.5, 0.8) samples, sintered at 1010, 1075 and 1120 °C, respectively.

Samples	**X-ray peak profile analyses**							
	Scherrer Method	Modified Scherrer method	Williamson-Hall plot			Size-strain plot		
	Crystallite size (D) in nm	D (nm)	D (nm)	Lattice Strain (ε)	Error	D (nm)	Lattice Strain (ε)	Error
$Na_{0.2}K_{0.8}NbO_3$	18	22	27	2.3×10^{-3}	0.8×10^{-3}	17	0.2×10^{-3}	$.07 \times 10^{-3}$
$Na_{0.5}K_{0.5}NbO_3$	19	26	50	3.8×10^{-3}	1.1×10^{-3}	28	2.2×10^{-3}	0.9×10^{-3}
$Na_{0.8}K_{0.2}NbO_3$	18	22	29	2.7×10^{-3}	1.3×10^{-3}	16	-	-

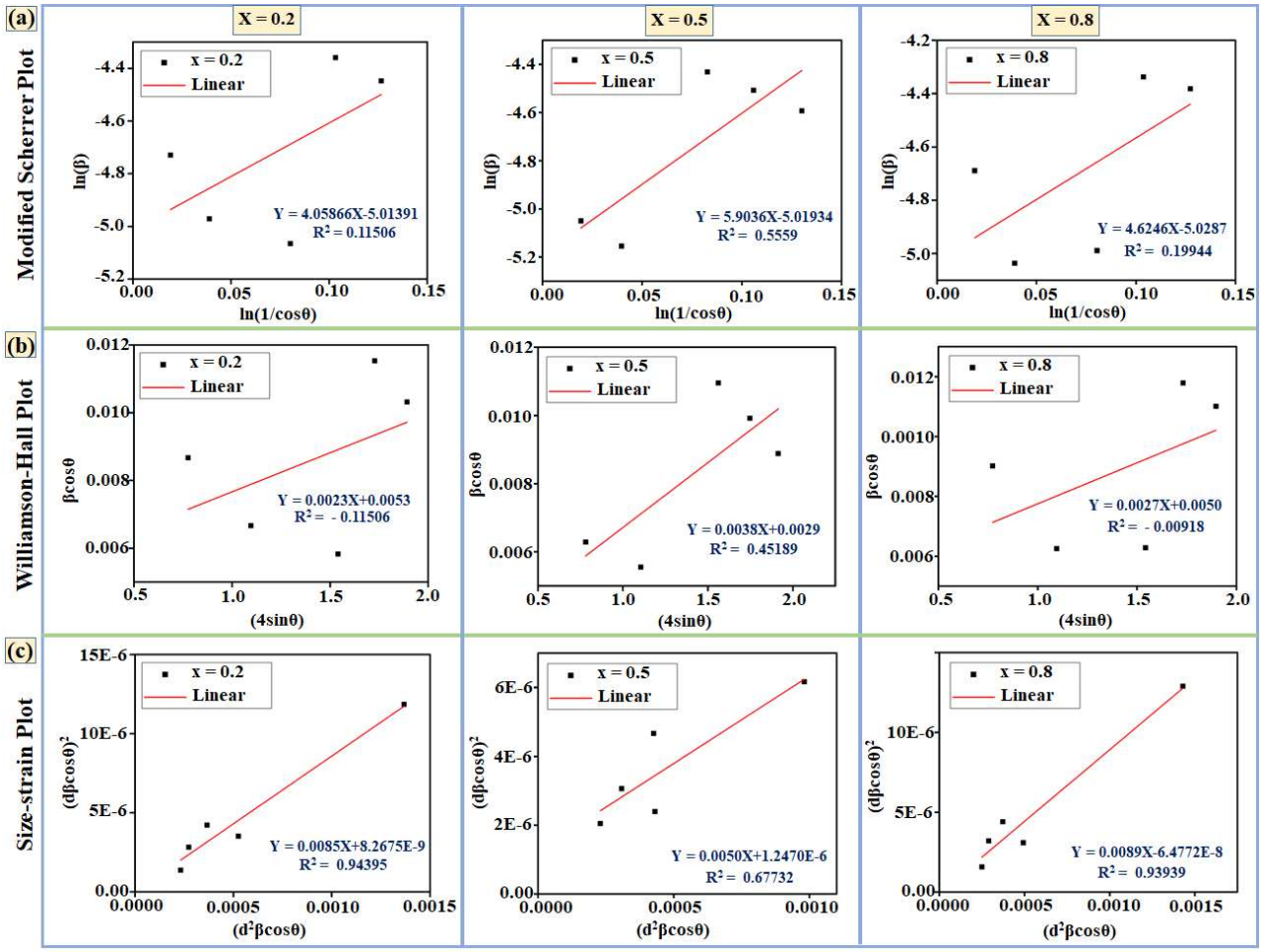

Fig. 4.3. X-ray peak profile analyses for $Na_xK_{1-x}NbO_3$ (x = 0.2, 0.5, 0.8) samples. Representation of plots obtained from (a) Modified Scherrer, (b) Williamson-Hall, and (c) Size-strain methods for $Na_xK_{1-x}NbO_3$ samples.

4.1.3. Fourier transform infrared (FTIR) spectroscopy

FTIR spectra illustrated that the characteristics vibrational bands in $Na_xK_{1-x}NbO_3$ for x = 0.2, 0.5 and 0.8 are observed at about 515, 546 and 532 cm^{-1}, respectively which corresponds to octahedron band of Nb-O [13] [Fig. 4.4]. In HA, FTIR spectra indicated the presence of vibrational bands of PO_4^{3-} (at ~ 1090, 1024, 962, 600 and 563 cm^{-1}), OH^- (at ~ 3572 and 631 cm^{-1}), CO_3^{2-} (at ~ 1458 and 1412 cm^{-1}) and HPO_4^{2-} (at ~ 874 cm^{-1}) [14, 15, 16, 17, 18] [Fig. 4.4]. Therefore, FTIR analyses further confirms the formation of phase pure NKN and HA.

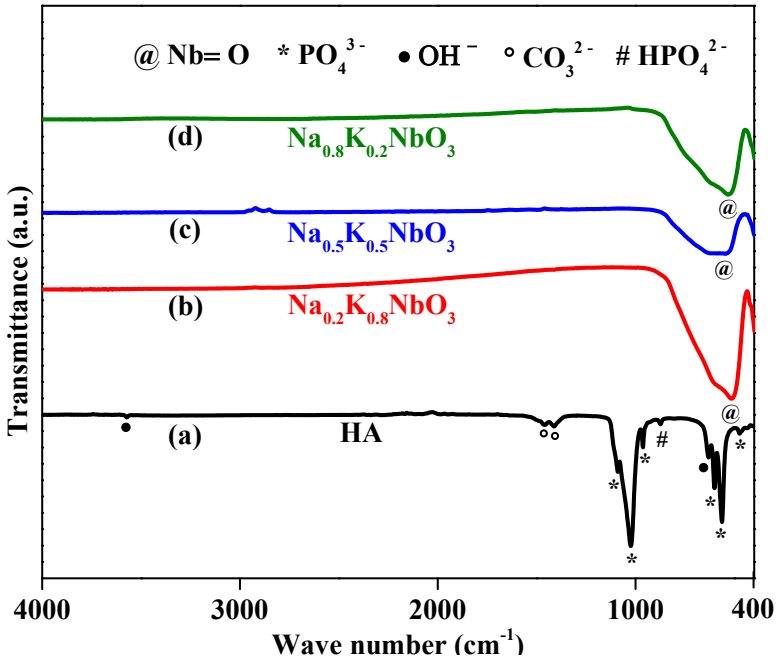

Fig. 4.4. FTIR spectra of the sintered HA and $Na_xK_{1-x}NbO_3$ (x = 0.2, 0.5 and 0.8) samples.

4.2. Microstructural analysis

The SEM micrographs and EDS spectra for $Na_xK_{1-x}NbO_3$ (x = 0.2, 0.5, 0.8) powders are shown in Fig. 4.5. The shape of the powders were observed to be almost polyhedral. The mean particle size of the calcined $Na_xK_{1-x}NbO_3$ (x = 0.2, 0.5, 0.8) powders are measured to be 630 ± 95 nm, 580 ± 75 nm and 470 ± 70 nm, respectively. Fig. 4.6 shows the SEM micrographs of the fractured $Na_xK_{1-x}NbO_3$ (x = 0.2, 0.5, 0.8) samples, sintered at 1010, 1075 and 1120 °C, respectively. The brittle mode of fracture are observed in all the samples. The size and distribution of porosity are almost similar for all the $Na_xK_{1-x}NbO_3$ (x = 0.2, 0.5, 0.8) samples.

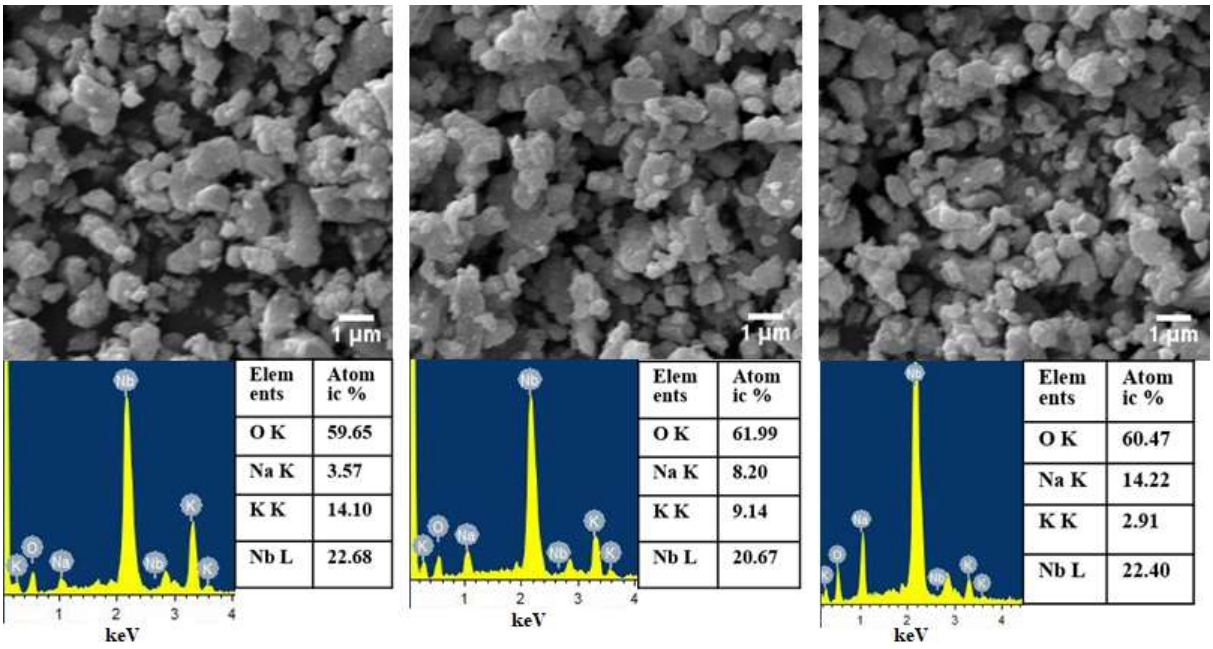

(a) *(b)* *(c)*

Fig. 4.5. Scanning electron microscopy (SEM) images and EDS graphs for $Na_xK_{1-x}NbO_3$ powders, (a) x = 0.2, (b) x = 0.5, (c) x = 0.8, calcined at 900 °C for 10 h.

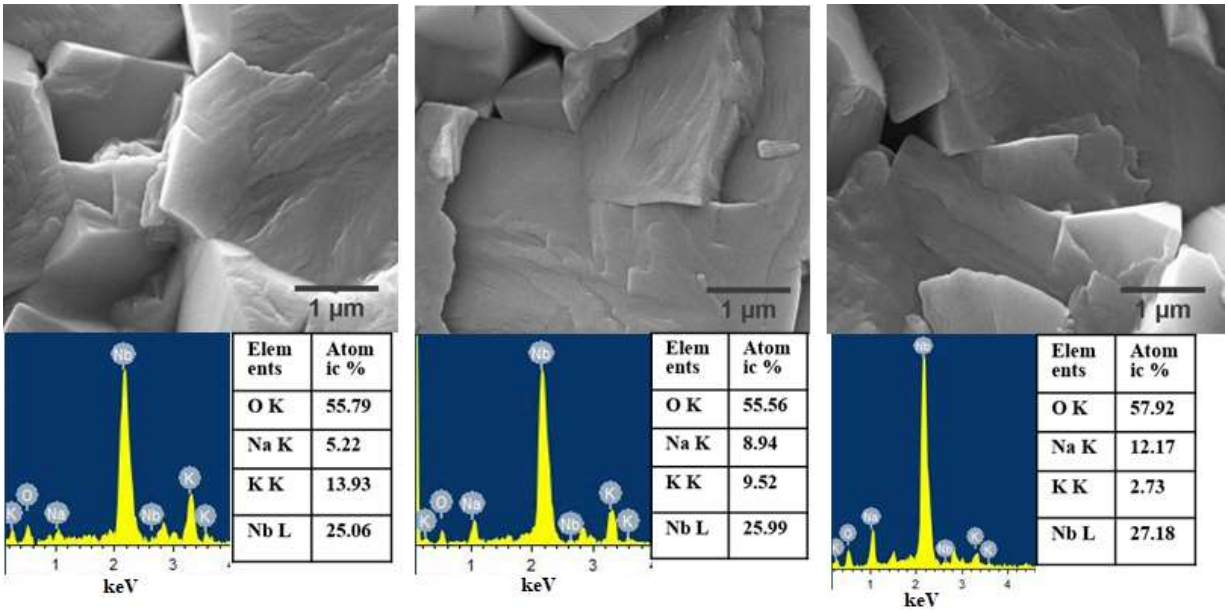

(a) *(b)* *(c)*

Fig. 4.6. Scanning electron microscopy (SEM) images and EDS graphs for fractured $Na_xK_{1-x}NbO_3$ samples, (a) x = 0.2, (b) x = 0.5, (c) x = 0.8, sintered at 1010, 1075 and 1120 °C, respectively.

4.3. Densification and mechanical property (Vicker's Hardness) measurement

The densification of $Na_xK_{1-x}NbO_3$ (x = 0.5) is difficult due to close solidus and liquidus temperature as 1140 ºC and 1280 ºC, respectively. However, the melting temperatures of $NaNbO_3$ and $KNbO_3$ intermediates have been reported to be 1420°C and 1040°C, respectively [19, 20]. In the present work, the sintering temperatures for $Na_xK_{1-x}NbO_3$ (x = 0.2, 0.5 and 0.8) have been optimized to be 1010, 1075 and 1120°C, respectively. The densification of sintered $Na_xK_{1-x}NbO_3$ samples for x = 0.2, 0.5 and 0.8 was measured to be 95.0 ± 0.5, 97.0 ± 0.4 and 95.0 ± 0.4 %, respectively.

Vicker's hardness and compressive strength were measured for sintered $Na_xK_{1-x}NbO_3$ (x = 0.2, 0.5, 0.8) and HA samples [Fig. 4.7]. The hardness values for $Na_{0.2}K_{0.8}NbO_3$, $Na_{0.5}K_{0.5}NbO_3$ and $Na_{0.8}K_{0.2}NbO_3$ are 5.8 ± 0.4, 6.5 ± 0.3 and 6.8 ± 0.4 GPa, respectively. However, the hardness value for HA sample is comparatively lower (4.7±0.4 GPa). The human bone has hardness value of (0.4 - 0.76 GPa) [21, 22, 23]. The maximum compressive strengths for $Na_{0.2}K_{0.8}NbO_3$, $Na_{0.5}K_{0.5}NbO_3$ and $Na_{0.8}K_{0.2}NbO_3$ are 121.73 ± 5.27, 128.05 ± 4.55 and 136.47 ± 5.86 MPa, respectively, which are comparatively higher than that of HA (81.65 ± 4.44 MPa) samples. The compressive strength for NKN samples is comparable to that of human bone (131 ± 20.7) MPa [24, 25]. The favorable mechanical properties reveal the potentiality of NKN ceramic to be used as a robust implant material.

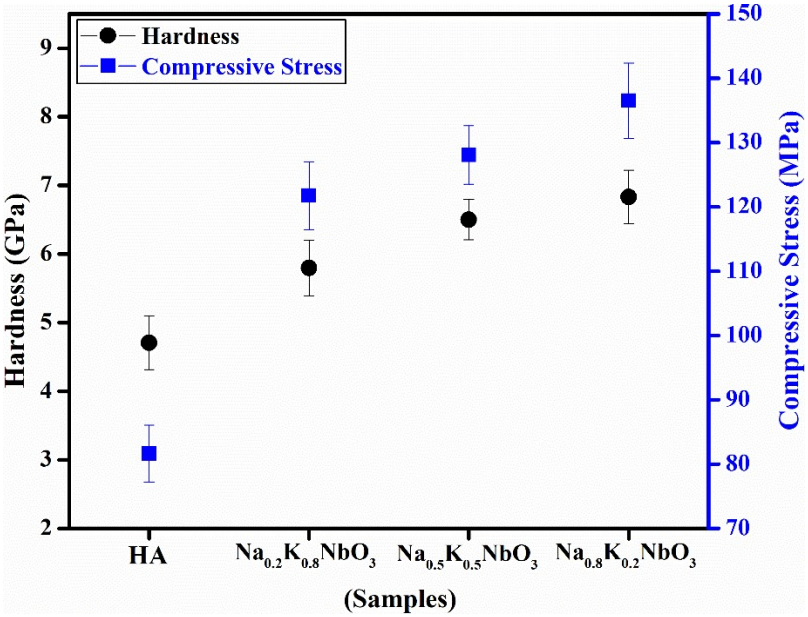

Fig. 4.7. Mechanical properties of $Na_xK_{1-x}NbO_3$ (x = 0.2, 0.5, 0.8) and HA samples. Hardness and compressive strength of sintered specimens of $Na_xK_{1-x}NbO_3$ and HA.

4.4. Leaching behavior of NKN pellets in biological fluid (SBF)

The ionic concentrations of Na^+ and K^+, leached from $Na_xK_{1-x}NbO_3$ (x = 0.2, 0.5, 0.8) after 7, 14 and 21 days of the immersion in SBF, are illustrated in Fig. 4.8. For Na-rich (i.e., $Na_{0.8}K_{0.2}NbO_3$) and K-rich (i.e., $Na_{0.2}K_{0.8}NbO_3$) samples, the leaching of Na^+ and K^+ initially increases up to 7 days and decreases thereafter. However, no significant leaching of these ions is observed in the composition with similar Na and K contents (i.e., $Na_{0.5}K_{0.5}NbO_3$). The maximum amount of leached Na^+ and K^+ for Na and K-rich compositions i.e., $Na_{0.8}K_{0.2}NbO_3$ and $Na_{0.2}K_{0.8}NbO_3$ are (Na^+: 608 ppm, K^+: 261 ppm) and (Na^+: 504 ppm, K^+: 400 ppm), respectively. However, this value for $Na_{0.5}K_{0.5}NbO_3$ is (Na^+: 445 ppm, K^+: 215 ppm).

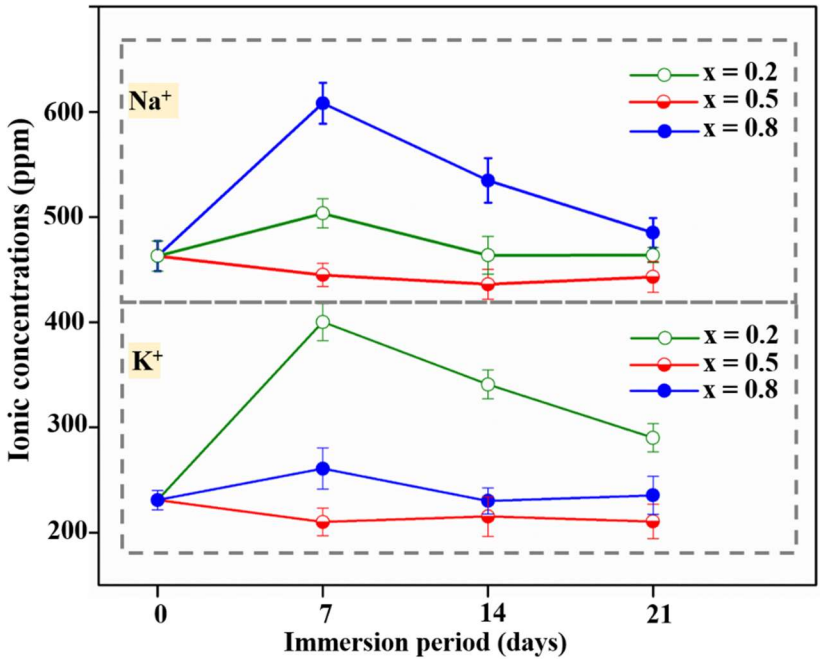

Fig. 4.8. Na^+ and K^+ leaching profiles from $Na_{0.x}K_{1-x}NbO_3$ (x = 0.2, 0.5, 0.8) in SBF. The plot represents the dynamic changes in concentrations of Na^+ and K^+, after immersion of $Na_xK_{1-x}NbO_3$ samples in SBF.

4.5. Charge measurement

The polarization induced surface charge on the $Na_xK_{1-x}NbO_3$ samples were measured from thermally stimulated depolarized current (TSDC) plot [Fig. 4.9] as [26];

$$Q = \frac{1}{\beta}\int I(T)dT \qquad (4.1)$$

Where, I, β and T are the current, heating rate (5 °C/min.) and temperature, respectively. The calculated surface charge densities for $Na_xK_{1-x}NbO_3$ (x = 0.2, 0.5, 0.8) samples are 0.515, 0.498 and 0.465 μC/cm^2, respectively.

The $Na_xK_{1-x}NbO_3$ exhibits the transitions of cubic to tetragonal ($T_{C-T,}$ Curie point) and monoclinic to tetragonal (T_{M-T}) phase, at the temperatures of ~ 420 and ~ 210 °C, respectively [2, 27, 28]. In our study, the TSDC spectra reveals the Curie point temperatures for $Na_xK_{1-x}NbO_3$ (x = 0.2, 0.5, 0.8) samples to be 425, 417 and 410 °C, respectively.

Moreover, the lower temperature phase transition is detected at the temperatures of 235, 229 and 221°C, respectively. Interestingly, a slight shift in phase transition temperatures towards the higher temperature region was observed with increasing the content of K which is in agreement with the previous study, performed for sodium potassium niobates mixed ceramic system [2].

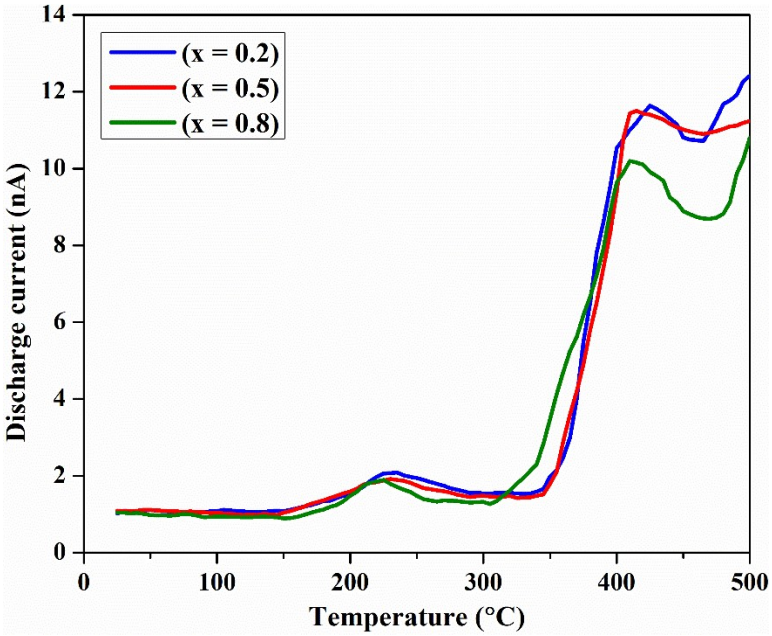

Fig. 4.9. Thermally stimulated depolarization current (TSDC) measurement. TSDC spectra of for $Na_xK_{1-x}NbO_3$ (x = 0.2, 0.5, 0.8) ceramics, polarized at 25 kV, followed by depolarization at the heating rate of 5 °C/min. upto 500 °C.

4.6. X-ray photoelectron spectroscopy (XPS) analyses

In XPS, the survey spectra demonstrating the binding energies of five elements on the surfaces of non-Pol. and polarized $Na_{0.5}K_{0.5}NbO_3$ samples i.e., Na (1s), K (2p), Nb (3p and 3d), C (1s) and O (1s) are shown in Fig. 4.10 (a). The peaks of binding energies for C 1s and Na 1s are observed at about 284.8 eV and 1071.1 eV, respectively, for both, non-Pol. and polarized samples. The binding energy peaks, corresponding to K 2p, Nb 3p and Nb 3d were

deconvoluted to ($2p_{1/2}$, $2p_{3/2}$), ($3p_{1/2}$, $3p_{3/2}$) and ($3d_{3/2}$, $3d_{5/2}$), which are found to be at about (295.1, 292.5 eV), (380.1, 365.1 eV) and (209.2, 206.5 eV), respectively, for both, non-Pol. and polarized samples of NKN. The binding energies of the observed orbitals C 1s, Na 1s, K 2p, Nb 3p and Nb 3d for non-Pol. and polarized NKN samples are close to the reported values for NKN [29, 30, 31]. The XPS spectra also reveals the Auger features of Na KLL and O KLL for non-Pol. and polarized NKN samples [Fig. 4.10 (a)] [31].

The XPS spectra of O 1s orbital scan for non-Pol. and polarized NKN samples are illustrated in Fig. 4.10 (b) and (c), respectively. The O 1s peak for non-Pol. NKN is deconvoluted into two peaks, centered at 529.4 eV [O 1s (I)] and 531.1 eV [O 1s (II)]. It has been reported that the highest intense peak (curve I) attributed to presence of oxygen in lattice state i.e., Nb-O bond in NKN ceramic [11, 32]. However, another peak (curve II) corresponds to the presence of oxygen vacancy [29, 33, 34, 35, 36, 37, 38]. The O 1s signal of polarized NKN sample is deconvoluted into three peaks, centered at 529.5 eV (lattice oxygen), 531.3 eV (oxygen vacancy) and 532.5 eV. The additional small peak at the higher binding energy side [O 1s (III)] is assigned to the adsorbed CO_2 or oxygen [11, 34, 36, 39, 40]. It can be clearly seen that the peak area, corresponding to the oxygen vacancy [O 1s (II)] for polarized NKN sample is larger than non-Pol. counter-part. Further, the ratios of the area under the curves representing the oxygen in lattice (curve I) and oxygen vacancy (curve II), calculated for non-Pol. and polarized NKN samples are 1.84 and 1.69, respectively. The low area ratio is indicating the accumulation of oxygen vacancies (about 9 %) on the polarized surface of NKN as compared to non-Pol. counter-part. It has been reported that the oxygen vacancies induced active sites on the surface facilitate the dissociative adsorption of water and therefore, makes the surface hydrophilic [41, 42, 43, 44]. Therefore, high-resolution O1s

spectra of polarized NKN reveals that the surface polarization enhanced the hydrophilicity, which augment the cellular functionality [45, 46, 47]. Apart from these results, the similar peak positions of Na, K and Nb for non-Pol. and polarized samples reveal that the polarization treatment did not alter the surface chemistry of NKN sample.

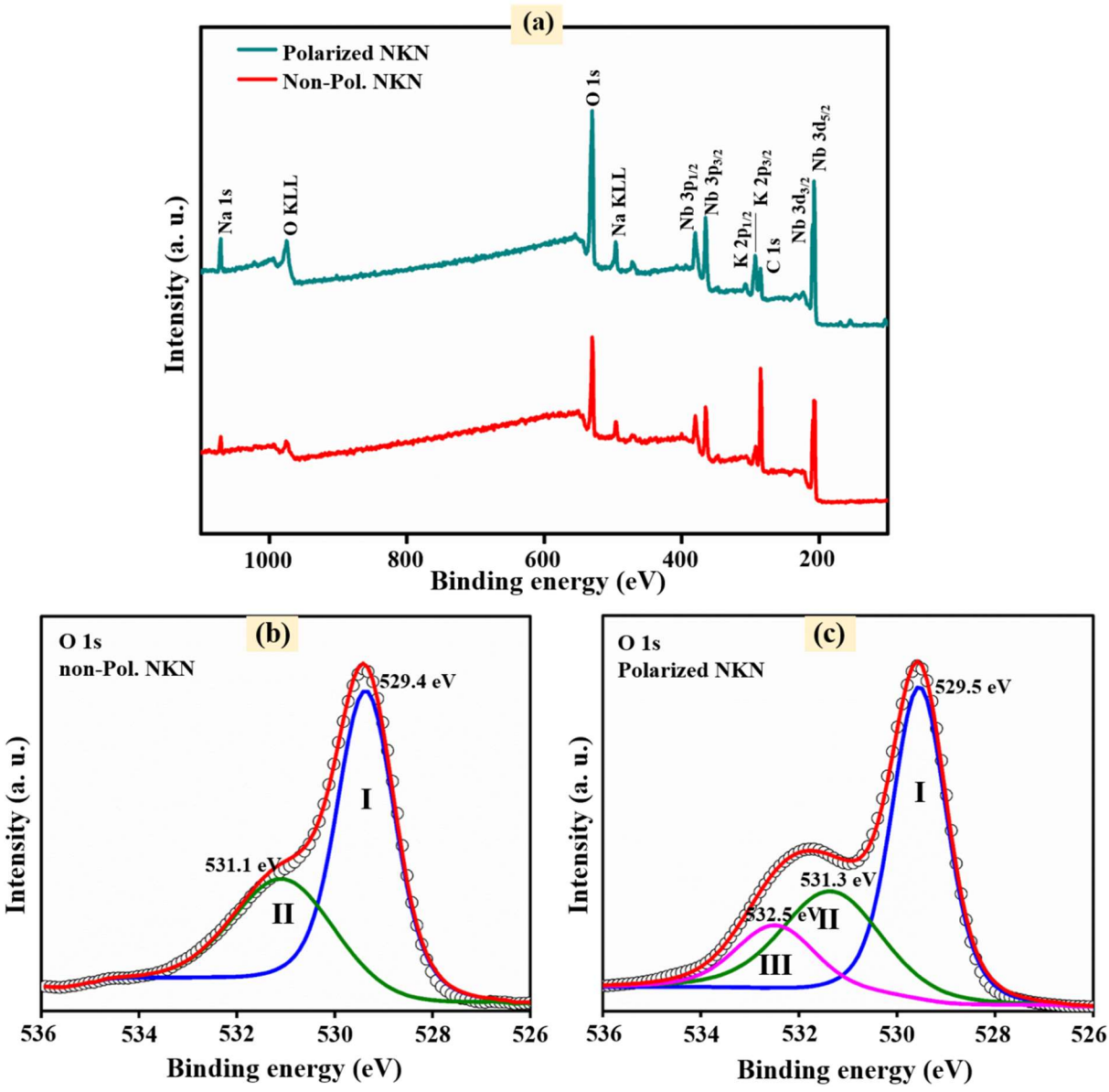

Fig. 4.10. XPS spectra for non-Pol. and polarized surfaces of NKN. (a) XPS survey spectrum of non-Pol. and polarized NKN for Na (1s), K (2p), Nb (3p), Nb (3d), C (1s) and O (1s)

orbitals states. (b) and (c) represent the O 1s XPS spectra for non-Pol. and polarized NKN samples, respectively.

4.7. Contact angle measurement

The influence of polarization charge on the surface wettability was assessed by the measurement of contact angle with DI water and DMEM media [Figs. 4.11 (a) and (b)]. The contact angles were observed to be significantly reduced on the polarized (both, positive and negative) surfaces of $Na_xK_{1-x}NbO_3$ (x = 0.2, 0.5, 0.8) and control samples, which indicates the polarization induced hydrophilicity. In addition, Neg. Pol. samples reveal the smallest contact angle i.e. highest hydrophilicity as compared to Pos. Pol. and non-Pol. samples. For Neg. Pol. $Na_xK_{1-x}NbO_3$ (x = 0.2, 0.5, 0.8) surfaces, the contact angle reduced by 54, 40, 59 % than that of the non-Pol. HA. Whereas, Neg. Pol. surface of HA sample show comparatively small reduction in contact angle (21 % than that of the non-Pol. HA), as measured in DI water. Similar trend is observed in DMEM media, where the contact angles on the Neg. Pol. surfaces of $Na_xK_{1-x}NbO_3$ (x = 0.2, 0.5, 0.8) samples are reduced by 53, 46, 57 % than that of the non-polarized HA. However, Neg. Pol. surface of HA demonstrates only 14 % reduction than that of the non-Pol. HA. Among all three Neg. Pol. NKN samples, Na and K-rich NKN i.e., $Na_{0.8}K_{0.2}NbO_3$ and $Na_{0.2}K_{0.8}NbO_3$ compositions are revealing comparatively higher hydrophilicities than $Na_xK_{1-x}NbO_3$ (x = 0.5). The hydrophilic surfaces are more favorable for the cellular growth and proliferation as compared to hydrophobic surfaces [45, 47, 48]. The contact angle measurement demonstrates enhanced hydrophilicity of the polarized surfaces of NKN as compared to non-Pol. surfaces, which is in well agreement with the outcomes of XPS analyses. XPS analyses reveal the accumulation of about 9 % of oxygen deficiency in negatively polarized surface of $Na_{0.5}K_{0.5}NbO_3$, which results in 25 % (with DI water) and 35

% (with DMEM media) decrease in contact angle for negatively polarized surface of $Na_{0.5}K_{0.5}NbO_3$ than its non-polarized counter-part.

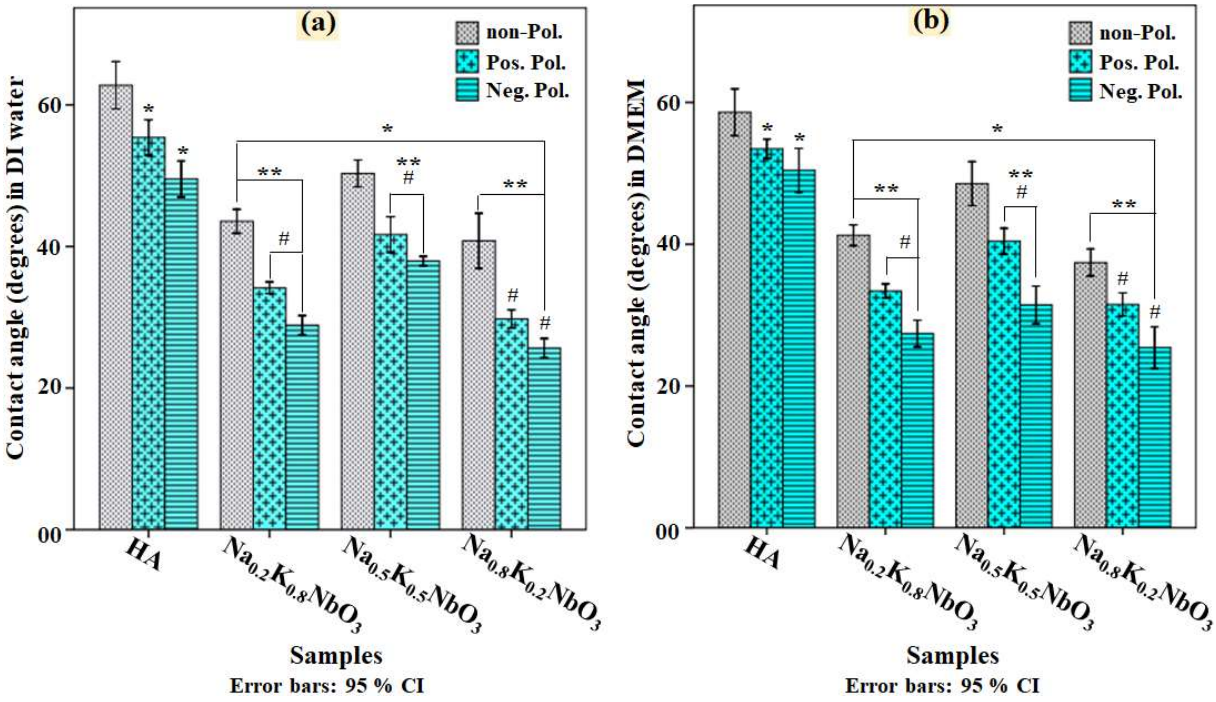

Fig. 4.11. Influence of surface polarization charge on hydrophilicity. The contact angle (°) values for non-Pol. and polarized surfaces of $Na_xK_{1-x}NbO_3$ (x = 0.2, 0.5, 0.8) and HA in (a) DI water and (b) DMEM media. (*) mark indicates the significant difference at $p \leq 0.05$, among the mean values of water contact angle on non-Pol. / polarized NKN and polarized HA samples in comparison to non-Pol. HA. (**) and (#) marks indicate the significant difference at $p \leq 0.05$, among the mean values of water contact angle on polarized NKN samples in comparison to Neg. Pol. HA and corresponding non-Pol. NKN samples, respectively.

4.8. Cellular response

4.8.1. Polarization induced early-stage cell adhesion

The florescence images of osteoblast like MG-63 cells, adhered on non-Pol. and polarized $Na_xK_{1-x}NbO_3$ and HA control, after 6 h of incubation, are shown in Fig. 4.12. The cells,

adhered on the NKN samples, are found to be more flattened and elongated than those on the HA samples. In addition, the polarized surfaces of NKN and control samples are observed to reveal larger sized adhered cells than their non-Pol. counter-part [Fig. 4.12 (a)]. The statistical analyses demonstrate that the cells, adhered on the Neg. Pol. $Na_xK_{1-x}NbO_3$ samples are significantly larger in size than those on the non-Pol. and polarized HA samples as well as their corresponding non-Pol. NKN samples [Fig. 4.12 (b)]. The mean projected area of the cells, adhered on the Neg. Pol. $Na_xK_{1-x}NbO_3$ (x = 0.2, 0.5, 0.8) samples are measured to be 2.3, 2.1, 2.6 times higher than those on the non-Pol. HA. In addition, Pos. Pol. and non-Pol. $Na_xK_{1-x}NbO_3$ (x = 0.2, 0.5, 0.8) samples reveal the mean projected area of adhered cells as (1.9, 1.8, 2.1 times of non-Pol. HA) and (1.7, 1.5, 1.8 times of non-Pol. HA), respectively. However, no significant difference in projected area of adhered cells is observed in non-Pol., Pos. Pol. and Neg. Pol. HA samples. Among different compositions of NKN, Neg. Pol. Na-rich NKN i.e., $Na_{0.8}K_{0.2}NbO_3$ and K-rich NKN i.e., $Na_{0.2}K_{0.8}NbO_3$ samples, not only exhibiting comparatively larger projected area of adhered cells than Neg. Pol. $Na_{0.5}K_{0.5}NbO_3$, but also demonstrating significant increase in the projected area of adhered cells than their respective Pos. Pol. NKN samples [Fig. 4.12 (b)]. However, no significant difference is observed among projected area of adhered cells on Neg. and Pos. Pol. surfaces $Na_{0.5}K_{0.5}NbO_3$. Overall, this result demonstrates that the surface polarization accelerates the early-stage adhesion of cells, preferably on the Neg. Pol. surfaces of Na and K-rich compositions of NKN.

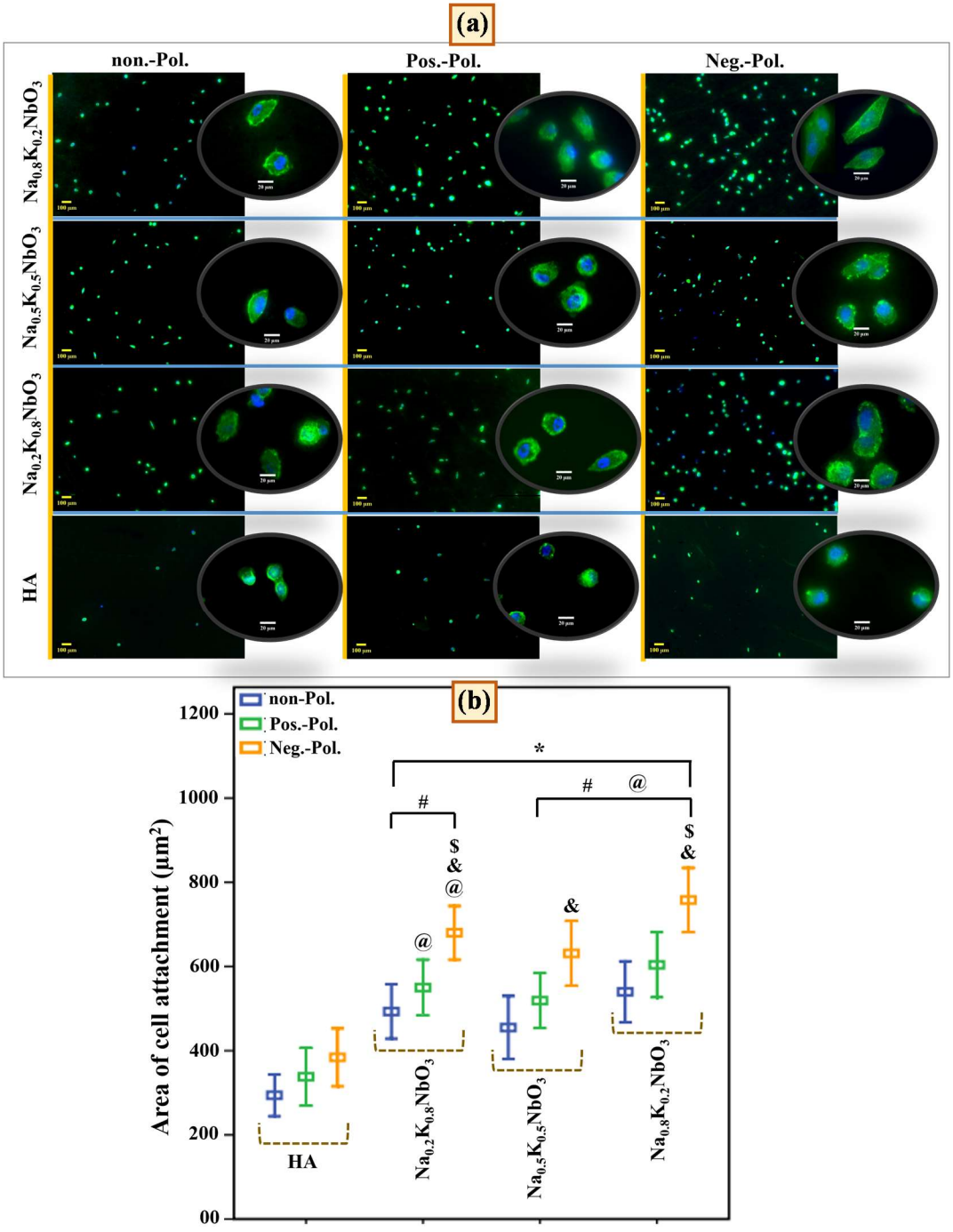

Fig. 4.12. Influence of polarization on early-stage adhesion (after 6h) of MG-63 cells. (a) The representative florescence images of MG-63 cells, adhered on non-Pol. and polarized $Na_xK_{1-x}NbO_3$ and control samples. (b) The plot, representing the projected area of the adhered cells (n = 20), on the non-Pol. and polarized NKN and control samples. (*), (#) and

(@) marks indicate the significant difference at $p \leq 0.05$, among the mean projected area of adhered cells on the non-Pol. and polarized $Na_xK_{1-x}NbO_3$ samples in comparison to the non-Pol., Pos. Pol. and Neg. Pol. control, respectively. (&) and ($) marks indicate the significant difference at $p \leq 0.05$, among the mean projected area of cells, adhered on the Neg. Pol. $Na_xK_{1-x}NbO_3$ samples in comparison to their respective non-Pol. and Pos. Pol. NKN samples, respectively.

4.8.2. Combined effect of surface polarization and dynamic electrical stimulation

The synergistic contribution of surface polarization charge and dynamic pulsed electrical stimulation on the osteogenic response of piezoelectric $Na_xK_{1-x}NbO_3$ (x = 0.2, 0.5, 0.8) samples and HA control have been assessed using MTT assay, ALP activity, florescence imaging and intracellular calcium ions measurement.

4.8.2.1. MTT assay

The viability of MG-63 cells and hMSCs on the non-treated and electrostatic and dynamic pulsed electric field treated $Na_xK_{1-x}NbO_3$ samples and control were quantitatively measured in terms of cell proliferation [Fig. 4.13]. Irrespective of any treatment, the cell viability is observed to be increase as the incubation period increases, for all the examined compositions. The treated NKN samples are demonstrating significantly higher viability for both of the cells as compared to treated HA samples, throughout the incubation period of 7 days. The Neg. Pol. $Na_xK_{1-x}NbO_3$ samples are revealing higher viability of MG-63 cells and hMSCs than their corresponding non-Pol. and Pos. Pol. NKN samples after 3, 5 and 7 days of incubation. This result is in agreement with the results, obtained from previous section (4.8.1). Interestingly, after 7 days of incubation, the dynamic pulsed electrical stimulation significantly enhances the viability, while the cells are being adhered on the charged NKN

samples as compared to the cellular response on mere charged surfaces [Figs. 4.13 (a) and (b)]. Overall, it can be clearly observed that the synergistically (electrostatic and dynamic electric field) treated NKN samples are showing maximum viability for both, MG-63 cells and hMSCs, throughout the study period. Among different compositions of NKN, the viability of MG-63 cells on the Neg. Pol. and electrically stimulated Neg. Pol. (E. S. Neg.) surfaces of $Na_xK_{1-x}NbO_3$ (x = 0.2, 0.5, 0.8) samples are measured to be (156, 148, 160 % of non-Pol. HA samples) and (172, 165, 190 % of non-Pol. HA samples), respectively, after 7 days of incubation. However, the viabilities of hMSCs are measured to be (183, 146, 191 % of non-Pol. HA samples) and (213, 196, 234 % of non-Pol. HA samples) on the Neg. Pol. and E. S. Neg. $Na_xK_{1-x}NbO_3$ (x = 0.2, 0.5, 0.8) samples, respectively, for the similar incubation period. It can be clearly seen that E. S. Neg. Na-rich NKN i.e., $Na_{0.8}K_{0.2}NbO_3$ and K-rich NKN i.e., $Na_{0.2}K_{0.8}NbO_3$ are showing highest viability of MG-63 cells and hMSCs than $Na_{0.5}K_{0.5}NbO_3$ samples, after 7 days of incubation.

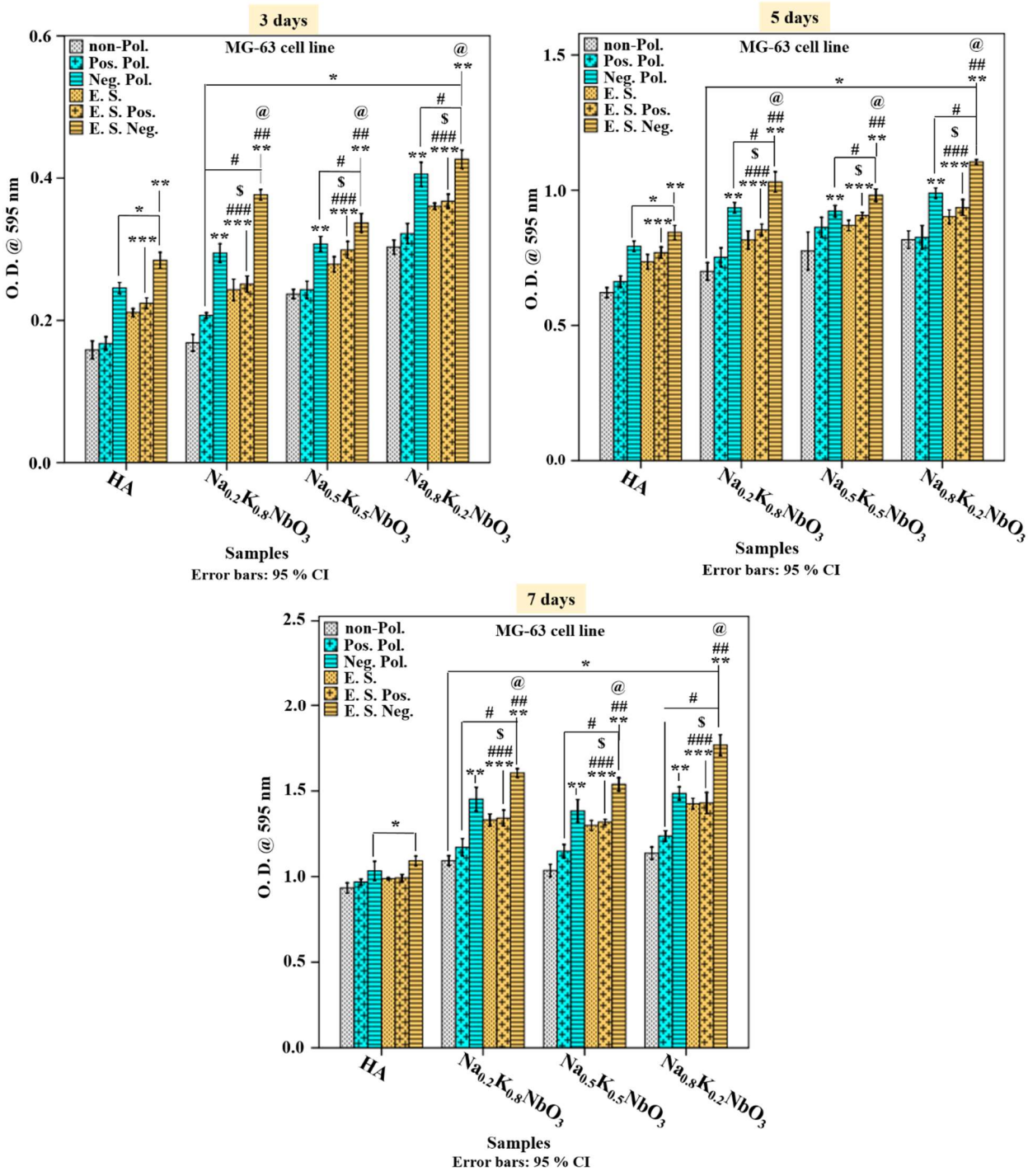
3 days
5 days
7 days
MG-63 cell line
non-Pol.
Pos. Pol.
Neg. Pol.
E. S.
E. S. Pos.
E. S. Neg.
O. D. @ 595 nm
HA
Na0.2K0.8NbO3
Na0.5K0.5NbO3
Na0.8K0.2NbO3
Samples
Error bars: 95 % CI

(a)

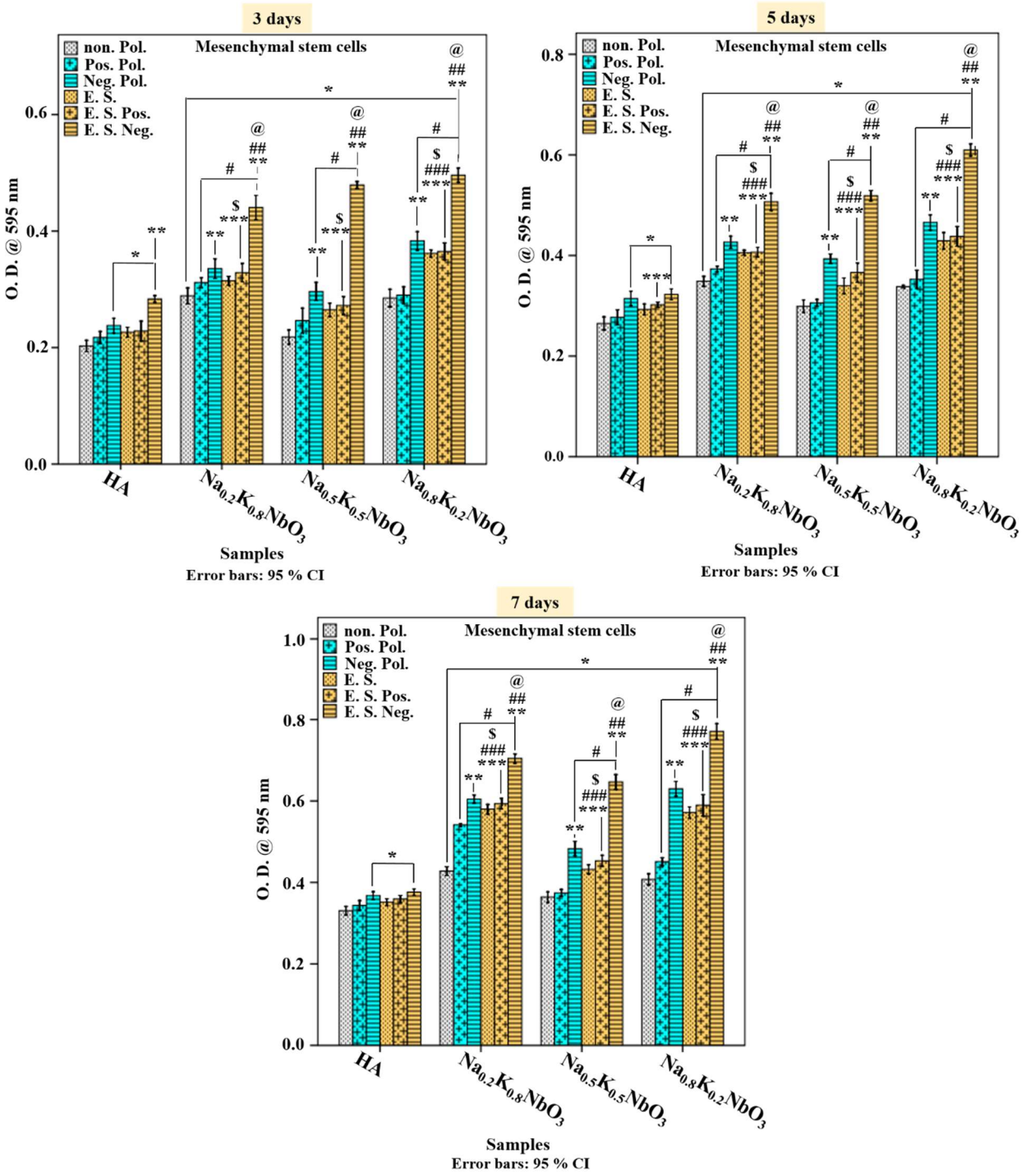

(b)

Fig. 4.13. Quantitative cellular response on non-treated and treated NKN and control samples. The plots representing the quantitative cellular response, using (a) MG-63 cells and (b) hMSCs, on non-Pol. and polarized $Na_xK_{1-x}NbO_3$ (x = 0.2, 0.5, 08) and control samples in

presence and absence of dynamic pulsed electrical stimulation. (*) mark indicates the significant difference at $p \leq 0.05$, among the mean values of optical density (O. D.) on all the non-treated and treated (Electrostatic/dynamic pulsed electrical stimulation) NKN and HA samples in comparison to non-Pol. HA, (#) mark denotes the significant difference at $p \leq 0.05$, among the mean values of O. D. on all the treated NKN samples in comparison to their respective non-Pol. NKN samples, (**) mark indicates the significant difference at $p \leq 0.05$, among the mean values of O. D. on Neg. Pol. NKN, electrically stimulated Neg. Pol. (E. S. Neg.) NKN and E. S. Neg. HA samples in comparison to Neg. Pol. HA. (##) and (@) symbols indicate the significant difference at $p \leq 0.05$, among the mean values of O. D. on E. S. Neg. NKN samples in comparison to their corresponding Neg. Pol. NKN and E. S. Neg. HA samples, respectively. (***) mark denotes the significant difference at $p \leq 0.05$, among the mean values of O. D. on the electrically stimulated Pos. Pol. (E. S. Pos.) NKN and HA samples in comparison to Pos. Pol. HA samples. (###) and ($) symbols indicate the significant difference at $p \leq 0.05$, among the mean values of O. D. on E. S. Pos. NKN samples in comparison to their corresponding Pos. Pol. NKN and E. S. Pos. HA samples, respectively.

4.8.2.2. Alkaline phosphatase (ALP) activity assessment

The ALP activity of MG-63 cells on non-treated and treated (Electrostatically/dynamically stimulated) piezoelectric $Na_xK_{1-x}NbO_3$ samples and control is represented in Fig. 4.14. After 7 days of incubation, the measured ALP activities are observed to be significantly higher on all of the non-treated and treated NKN samples (except non-Pol. $Na_{0.5}K_{0.5}NbO_3$) as compared to non-treated as well as treated HA control [Fig. 4.14 (a)]. However, after 14 days of cell seeding, entire examined compositions of NKN (irrespective of treatment methods) exhibit

significant increase in ALP activity for MG-63 cells [Fig. 4.14 (b)]. It can be clearly seen that the Neg. Pol. NKN samples are representing significantly higher ALP activities than the positively as well as non-Pol. surfaces of their respective compositions of NKN. Interestingly, the application of dynamic pulsed electrical stimulation over polarized surfaces further enhanced the ALP activity and consequently, resulted in significant increase in the ALP activity as compared to the respective polarized NKN samples, cultured in the absence of electrical stimulation [Figs. 4.14 (a) and (b)]. The maximum ALP activity is observed on the electrically stimulated Neg. Pol. (E. S. Neg.) NKN samples, among all of the non-treated and treated samples. This finding indicates that the synergistic action of electrostatic-dynamic electrical stimulation considerably promoted earlier differentiation of osteoblast like MG-63 cells. After 14 days of cell seeding, the values of ALP activity on the Neg. Pol. and E. S. Neg. $Na_xK_{1-x}NbO_3$ (x = 0.2, 0.5, 0.8) samples are measured to be (3.28, 3.08, 3.38 times of non-Pol. HA) and (3.71, 3.47, 4.13 times of non-Pol. HA), respectively. However, these values on the Neg. Pol. and E. S. Neg. HA samples are (1.27 times of non-Pol. HA) and (1.51 times of non-Pol. HA), respectively. From above results, it can be clearly seen that E. S. Neg. Na-rich NKN i.e., $Na_{0.8}K_{0.2}NbO_3$ and K-rich NKN i.e., $Na_{0.2}K_{0.8}NbO_3$ samples are significantly promoting the osteogenic differentiation as compared to E. S. Neg. $Na_{0.5}K_{0.5}NbO_3$ samples.

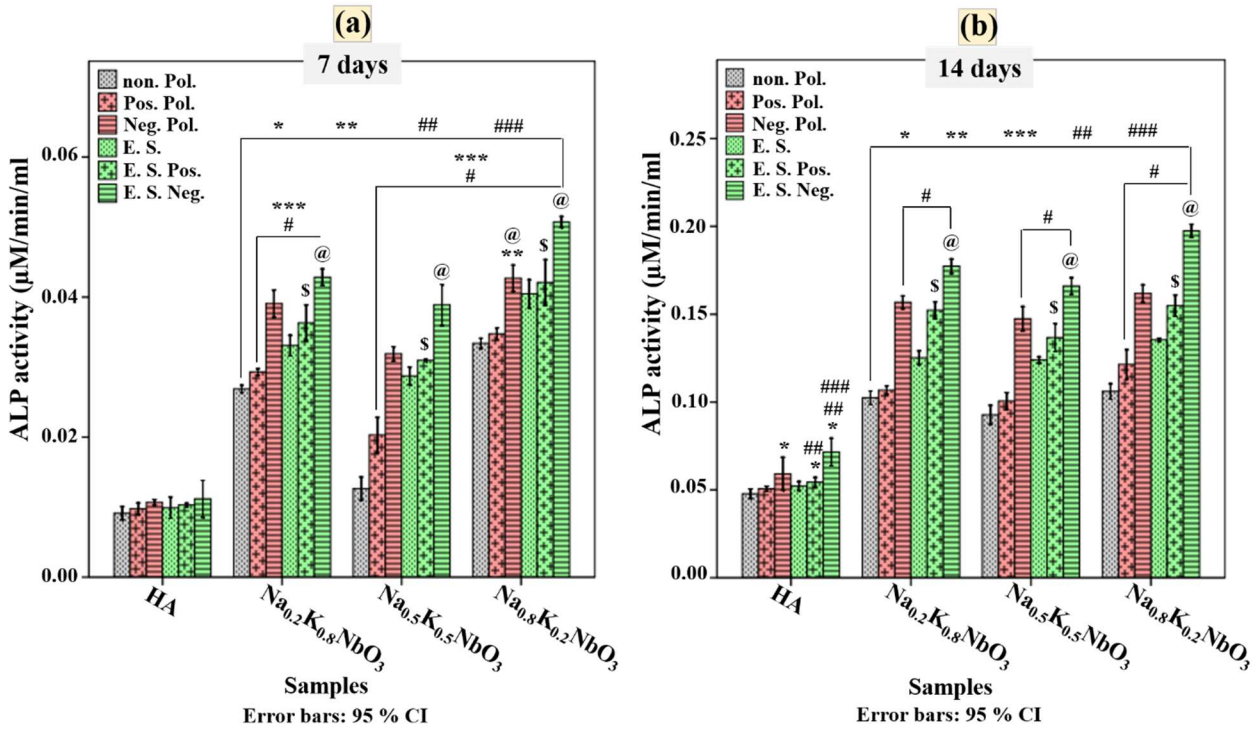

Fig. 4.14. Osteogenic differentiation response of non-treated and treated piezoelectric NKN and control samples. The plot illustrating the alkaline phosphatase (ALP) activity on the non-Pol., electrostatically (Pos. and Neg. Pol.) – electrically stimulated (dynamic) Pos. Pol. (E. S. Pos.) and electrically stimulated (dynamic) Neg. Pol. (E. S. Neg.) $Na_xK_{1-x}NbO_3$ (x = 0.2, 0.5, 0.8) and HA samples, after (a) 7 and (b) 14 days. (*), (##), (###) symbols indicate the significant difference at $p \leq 0.05$, among the mean ALP activity on all of the non-treated and treated NKN and HA samples in comparison to non-Pol., Pos. Pol. and E. S. Pos. HA samples, respectively. (**), (***) symbols indicate the significant difference at $p \leq 0.05$, among the mean ALP activity on all of the NKN samples in comparison to Neg. Pol. and E. S. Neg. HA, respectively. (#) mark indicates the significant difference at $p \leq 0.05$, among the mean ALP activity on all of the treated NKN samples in comparison to their corresponding non-Pol. NKN samples. (@) mark indicates the significant difference at $p \leq 0.05$, among the mean ALP activity on all of the E. S. Neg. NKN samples in comparison to their respective

Neg. Pol. NKN. ($) mark indicates the significant difference at $p \leq 0.05$, among the mean ALP activity on all of the E. S. Pos. NKN samples in comparison to their corresponding Pos. Pol. NKN samples, respectively.

4.8.2.3. Morphological analyses of adhered cells

The response of the hMSCs on the non-treated and treated (Electrostatically/dynamically stimulated) piezoelectric $Na_xK_{1-x}NbO_3$ samples and control were qualitatively measured in terms of morphology and projected area of adhered cells, as illustrated in Figs. 4.15 (a) and (b). It can be clearly seen that the dynamic pulsed electric field treated non-Pol. or polarized NKN samples and the Neg. Pol. NKN samples reveal elongated morphology of adhered hMSCs [Fig. 4.15 (a)]. In addition, well organized polygon shaped and more elongated morphology of adhered cells can be observed on the electrically stimulated Neg. Pol. (E. S. Neg.) NKN samples than their respective non-Pol., polarized (Pos. or Neg. Pol.), E. S. and E. S. Pos. samples. The area measurement analyses of adhered cells further revealed that the treated piezoelectric NKN samples demonstrate significantly higher spreading of adhered hMSCs than the control samples, treated with similar method [Fig. 4.15 (b)]. In addition, the Neg. Pol., electrically stimulated, E. S. Neg. and E. S. Pos. NKN samples are revealing significant increase in projected area of adhered hMSCs than non-Pol. NKN [Fig. 4.15 (b)]. Among different treated (Electrostatically/dynamically stimulated) NKN samples, the E. S. Neg. $Na_xK_{1-x}NbO_3$ (x = 0.2, 0.5, 0.8) samples demonstrate the highest area of adhered cells, which is measured to be (262, 250, 270 %) of mean projected area of hMSCs cells, adhered on non-Pol. HA samples [Fig. 4.15 (b)].

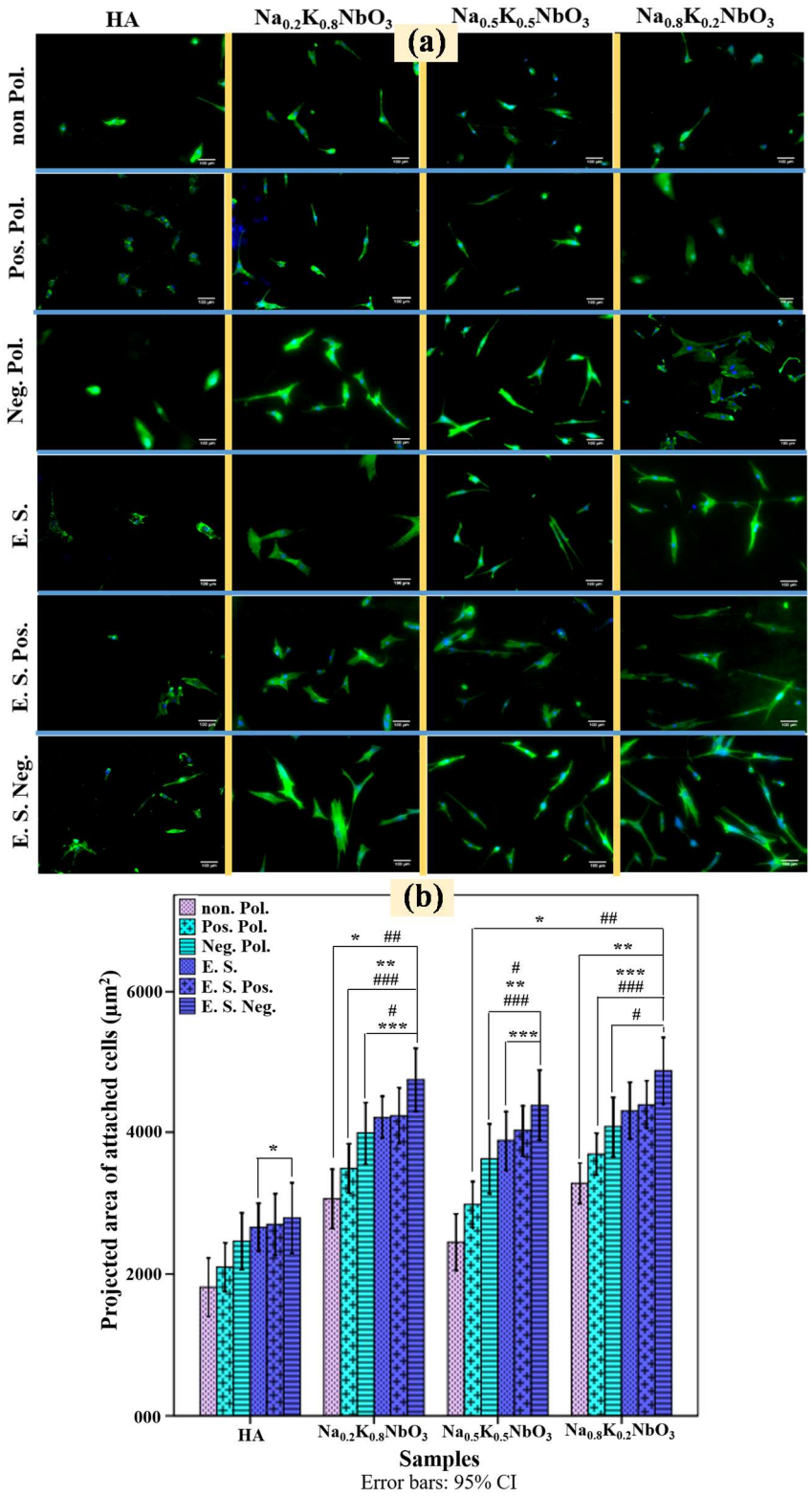

Fig. 4.15. Morphological analyses of adhered cells on non-treated and treated NKN and control samples. (a) Representative fluorescence microscopic images of stained hMSCs,

adhered on the non-treated and treated (Electrostatically/dynamically stimulated) piezoelectric $Na_xK_{1-x}NbO_3$ samples and control. (b) The plot represents the projected area of the adhered cells (n = 20) on non-treated and treated NKN samples and control. (*), (##), (###) symbols indicate the significant difference at $p \leq 0.05$, among the mean projected area of cells adhered on all of the non-treated and treated NKN and HA samples in comparison to non-Pol., Pos. Pol. and E. S. Pos. HA samples, respectively. (**), (***) symbols indicate the significant difference at $p \leq 0.05$, among the mean projected area of cells, adhered on all of the NKN samples in comparison to Neg. Pol. and E. S. Neg. HA, respectively. (#) symbol indicates the significant difference at $p \leq 0.05$, among the mean projected area of cells, adhered on all of the treated NKN samples in comparison to their respective non-Pol. NKN samples.

4.8.2.4 Intracellular Ca^{2+} measurement

The level of intracellular Ca^{2+} on non-treated and treated (Electrostatically/dynamically stimulated) piezoelectric $Na_xK_{1-x}NbO_3$ and control samples, using intracellular Ca^{2+} fluorescence indicator Fura-2 AM loaded MG-63 cells, are illustrated in terms of the mean of the peak values of the ratio of fluorescence intensity at 340 and 380 nm [Fig. 4.16]. The level of intracellular Ca^{2+} is found to be significantly higher on the non-Pol. and polarized NKN samples, cultured under dynamic pulsed electrical stimulation as compared to the non-Pol. and polarized control HA samples, cultured in the absence or presence of electrical stimulation [Fig. 4.16]. In addition, all of the Neg. Pol. and all of the dynamic electrically stimulated (E. S., E. S. Pos. and E. S. Neg.) samples are revealing significant rise in the level of intracellular Ca^{2+} as compared to the corresponding NKN samples [Fig. 4.16]. The level of intracellular Ca^{2+} on negatively polarized and all of the dynamic pulsed electrical stimulation

(Neg. Pol., E. S., E. S. Pos., E. S. Neg.) treated $Na_xK_{1-x}NbO_3$; x = 0.2, x = 0.5 and x = 0.8 samples are measured to be (2.1, 2, 2.2, 2.9 times of non-Pol. HA), (2.1, 2.1, 2, 2.7 times of non-Pol. HA) and (2.3, 2.2, 2.3, 3.1 times of non-Pol. HA), respectively. However, it is comparatively lower (1.5, 1.5, 1.6, 1.8 times of non-Pol. HA) on HA samples. Interestingly, the dynamic pulsed electrically stimulated Neg. Pol. Na-rich NKN i.e., $Na_{0.8}K_{0.2}NbO_3$ and K-rich NKN i.e., $Na_{0.2}K_{0.8}NbO_3$ samples are showing comparatively larger increase in the level of intracellular Ca^{2+} than similarly treated $Na_{0.5}K_{0.5}NbO_3$ samples, which is consistent with the cellular response on treated samples [Figs. 4.12, 4.13, 4.14 and 4.15]. Overall, the synergistic action of electrostatic-dynamic stimulation increases in concentration of Ca^{2+} in MG-63 cells and thereby, positively regulate the functionality of cells, cultured preferably on dynamic electrically stimulated Neg. Pol. NKN samples.

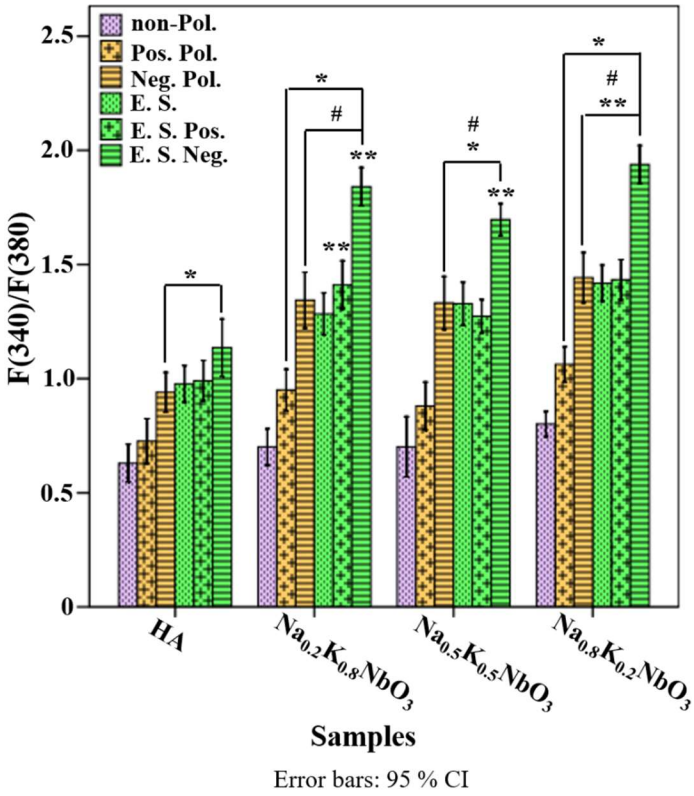

Fig. 4.16. The level of intracellular Ca^{2+} on non-treated and treated NKN and control samples, cultured with MG-63 cells. The plot representing the mean of the peak values of the

ratio of fluorescence intensity at 340 and 380 nm, measured for the cells loaded with intracellular Ca^{2+} indicator Fura-2 AM on the non-treated and treated (Electrostatically/dynamically stimulated) piezoelectric $Na_xK_{1-x}NbO_3$ samples and control. (*) mark indicates the significant difference at $p \leq 0.05$, among the mean of peak values of estimated ratio on Neg. Pol., E. S., E. S. Pos. and E. S. Neg. NKN as well as HA samples, in comparison to non-Pol. and polarized HA samples, cultured without dynamic electrical stimulation. (**) mark indicates the significant difference at $p \leq 0.05$, among the mean of peak values of estimated ratio on Neg. Pol., E. S., E. S. Pos. and E. S. Neg. NKN samples, in comparison to non-Pol. and polarized HA samples cultured with dynamic electrical stimulation. (#) mark indicates the same at $p \leq 0.05$, among non-Pol. and polarized NKN samples, cultured under dynamic electrical stimulation in comparison to their corresponding non-Pol. and polarized NKN samples, cultured without electrical stimulation.

4.9. Discussion

Overall, the above results clearly infers that the dynamic pulsed electrical stimulation on the cells, adhered on Neg. Pol. surfaces of Na-rich NKN ($Na_{0.8}K_{0.2}NbO_3$) and K-rich NKN ($Na_{0.2}K_{0.8}NbO_3$) samples revealed augmented cell adhesion, proliferation and differentiations [Figs. 4.12, 4.13, 4.14 and 4.15]. The Neg. Pol. surfaces of NKN exhibit significantly higher hydrophilicity as compared to the non-Pol. and Pos. Pol. respective NKN and HA control, in DI water and cell culture media [Fig. 4.11]. XPS analyses also revealed that the surface polarization facilitates the accumulation of oxygen vacancies which forms active sites for water adhesion and thereby, increases the surface hydrophilicity [Fig. 4.10] [41, 42, 43, 44]. The enhanced hydrophilicity of the Neg. Pol. surfaces augment cellular response [45, 47, 48, 49]. The Neg. Pol. surfaces attract the positively charged cations (Ca^{2+}, H^+ ions) from the

biological fluid which further attract the negatively charged proteins (fibronectin and integrin) and therefore, Neg. Pol. surfaces act as a stimulus for cellular adhesion and proliferation [Fig. 4.17 (a)] [48, 50]. In the present study, the dynamic pulsed electrical stimulation was applied, while the cells are being adhered on the polarized samples, after 12 and 24 h of culture. Previous studies reported that the local electric field in the extracellular matrix activates the voltage gated Ca^{2+} channels, present on the cellular membrane and changes the configuration of receptor channels in the endoplasmic reticulum [Fig. 4.17 (b)] [50, 51]. Consequently, the local electric field facilitates the influx of Ca^{2+} ions from extracellular microenvironment and endoplasmic reticulum. The increased concentration of intracellular Ca^{2+} ions activate calcium modulated protein and other relevant factors, responsible for the synthesis of bone morphogenic protein (BMP-2) and transforming growth factor (TGF-β), which helps in regulating cellular metabolism [50, 51, 52]. Therefore, the dynamic pulsed electrical stimulation and negatively charged polarization synergistically contributes in promoting the cellular adhesion, proliferation and differentiation.

Another noticeable key point is that the Na and K-rich compositions of NKN i.e., $Na_{0.8}K_{0.2}NbO_3$ and $Na_{0.2}K_{0.8}NbO_3$ are comparatively more favorable for the attachment and proliferation of MG-63 cells and hMSCs than $Na_{0.5}K_{0.5}NbO_3$ samples. The ion dissolution study using ICP analyses indicates that the concentration of Na^+ and K^+, leached in SBF was comparatively higher for Na and K-rich compositions i.e., $Na_{0.8}K_{0.2}NbO_3$ and $Na_{0.2}K_{0.8}NbO_3$ than $Na_{0.5}K_{0.5}NbO_3$ [Fig. 4.8]. The leaching of Na^+ or K^+ causes a slight increase in the pH of culture media which may be one of the major reasons for augmented cellular response on Na and K-rich compositions of NKN [53, 54, 55]. Overall, the synergistic action of surface polarization charge, dynamic pulsed electrical stimulation and optimized compositional

modification provides a novel pathway to improve the biological response of NKN piezobioceramics.

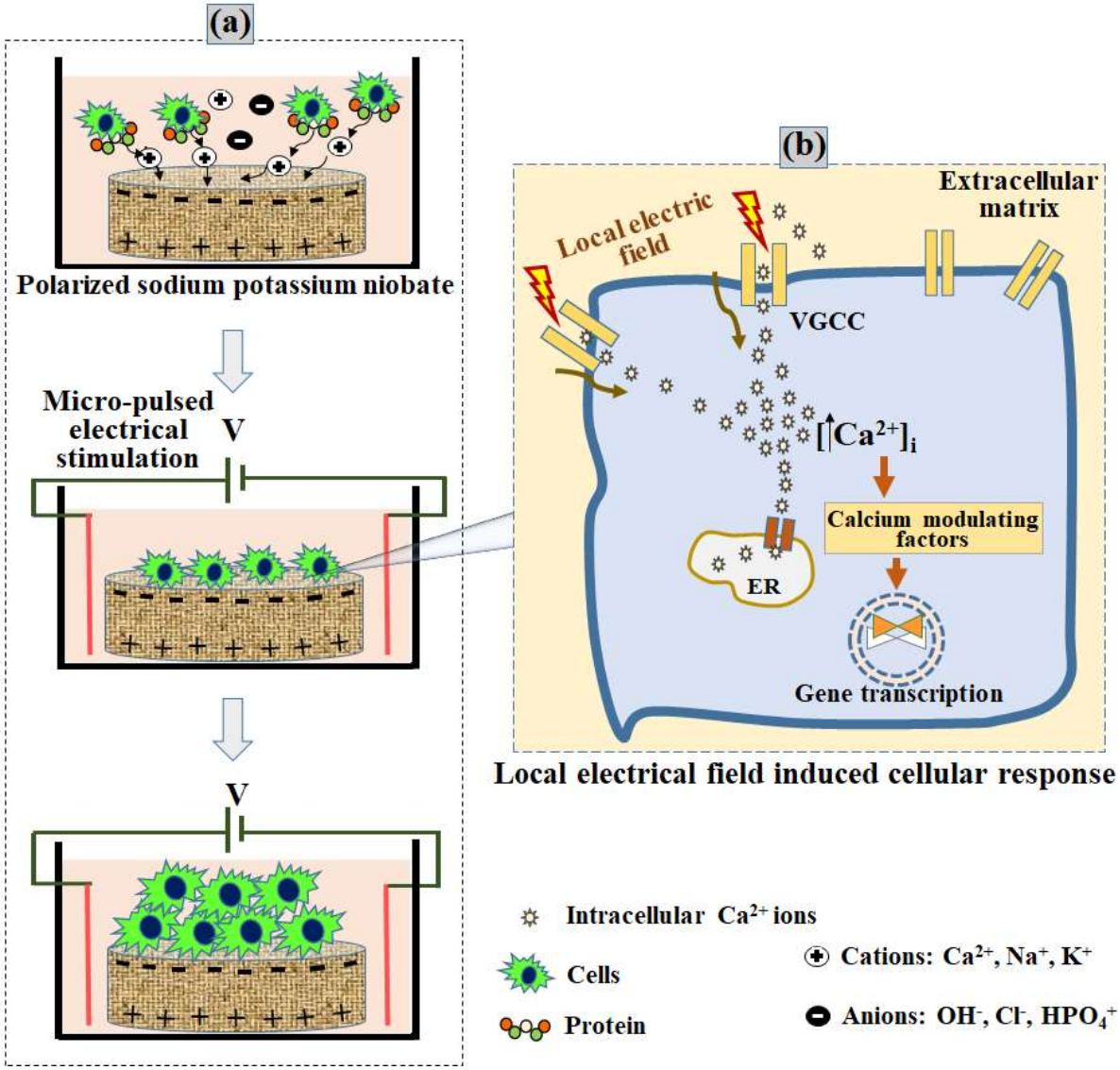

Fig. 4.17. Schematic demonstrating the synergized effect of Neg. Pol. surface and dynamic pulsed electrical stimulation in promoting cellular response of piezoelectric NKN. (a) The cations present in the culture media attract towards the Neg. Pol. surface and thereby, the adhered cations further attract negatively charged cell membrane and protein and consequently, promote cellular adhesion [50, 51]. In addition, hydrophilicity increases for the Neg. Pol. surface, which consequently, accelerates cellular functionality [48]. (b) The

piezoelectric charge and dynamic pulsed electrical stimulation induced local electric field activates the voltage gated Ca^{2+} channels which permits the influx of Ca^{2+} [50, 51]. The increased concentration of intracellular Ca^{2+} activates the calcium modulating factors which further results in gene transcription and therefore, assists in regulating cellular metabolism [50, 51].

In the present study, $Na_xK_{1-x}NbO_3$ (x = 0.2 - 0.8) samples reveal monoclinic geometry with space group P1m1 which was confirmed by Rietveld refinement analyses. The X-ray peak profile analyses revealed that the Na- ($Na_{0.8}K_{0.2}NbO_3$) and K- ($Na_{0.2}K_{0.8}NbO_3$) rich compositions of NKN are showing comparatively smaller crystallite size than $Na_{0.5}K_{0.5}NbO_3$. The Vicker's hardness and compressive strength of $Na_xK_{1-x}NbO_3$ (x = 0.2, 0.5, 0.8) samples are (123, 138, 145 %) and (149, 157, 167 %) of HA. ICP-AES analyses demonstrate comparatively higher leaching of Na^+ and K^+ in SBF, for Na and K-rich compositions of NKN, respectively. The negatively charged surfaces of NKN samples showed considerable improvement in surface hydrophilicity and remarkably promote early-stage cellular adhesion. The electrostatic surface polarization charge and dynamic pulsed electrical stimulation synergistically augments cellular proliferation, adhesion and differentiation, preferably on the Neg. Pol. surface of Na and K-rich compositions of NKN. The remarkable improvement in cellular activity on the electrostatic-dynamic electric field stimulated NKN samples occurs due to the modulation of metabolic signaling pathway of cells which was confirmed by the measurement of intracellular Ca^{2+} ions.

References

[1] R. D. Shannon, Revised effective ionic radii and systematic studies of interatomic distances in halides and chalcogenides, Acta Cryst. A 32 (1976) 751-767.

[2] J. Tellier, B. Malic, B. Dkhil, D. Jenko, J. Cilensek, M. Kosec, Crystal structure and phase transitions of sodium potassium niobate perovskites, Sol. Stat. Sci. 11 (2009) 320-324.

[3] C. Suryanarayana, M. G. Norton, X-ray diffraction: a practical approach. Plenum Press Publishing, New York (1998).

[4] S. Sarkar, R. Das, Shape effect on the elastic properties of Ag nanocrystals, Micro Nano Let. 13 (2018) 312–315.

[5] M. A. Tagliente, M. Massaro, Strain-driven (002) preferred orientation of ZnO nanoparticles in implanted silica, Nucl. Instrum. Methods Phys. Res. B. 266 (2008) 1055–1061.

[6] R. Jacob, J. Isac, X-ray diffraction line profile analyses of $Ba_{0.6}Sr_{0.4}Fe_xTi_{1-x}O_3$-δ, Int. J. Chem. Studies 2 *(*2015) 12-21.

[7] K. A. Zak, A. W. H. Majid, M. E. Abrishami, R. Yousefi, X-ray analysis of ZnO nanoparticles by Williamson-Hall and size-strain plot methods, Solid State Sci. 13 (2011) 251.

[8] M. Rabiei, A. Palevicius, A. Monshi, S. Nasiri, A. Vilkauskas, G. Janusas, Comparing Methods for Calculating Nano Crystal Size of Natural Hydroxyapatite Using X-Ray Diffraction, Nanomaterials 10 (2020) 1627.

[9] D. Hull, D. J. Bacon, Chapter 3 - Movement of Dislocations, Editor(s): D. Hull, D.J. Bacon, Introduction to Dislocations (Fifth Edition), Butterworth-Heinemann (2011) 43-62.

[10] T. O. Erinosho, F. P. E. Dunne, Lattice strain distributions due to elastic distortions and GND development in polycrystals, J. Mech. Phy. Solids 67 (2014) 62-86

[11] K. Shalini, N. V. Giridharan, Coexistence of electric polarization and magnetic ordering in acceptor doped potassium sodium niobate (KNN) ceramics, Mater. Res. Express 5 (2018) 09610.

[12] D. Nath, F. Singh, R. Das, X-ray diffraction analysis by Williamson-Hall, Halder-Wagner and size-strain plot methods of CdSe nanoparticles- a comparative study, Mat. Chem. Phy. 239 (2020) 122021

[13] D. Q. Zhang, Z. C. Qin, X. Y. Yang, H. B. Zhu, M. S. Cao, Study on synthesis and evolutionof sodium potassium niobate ceramic powders by an oxalic acid-based sol-gel method, J. Sol- Gel Sci. Tech. 57 (2011) 31-35.

[14] S. Raynaud, E. Champion, D. Bernache-Assollant, P. Thomas, Calcium phosphate apatites with variable Ca/P atomic ratio I. Synthesis, characterization and thermal stability of powders, Biomaterials 23 (2002) 1065-1072.

[15] H. Gheisari, E. Karamian, M. Abdellahi, A novel hydroxyapatite–Hardystonitenano composite ceramic, Ceram. Int. 41 (2015) 5967-5975.

[16] H. Li, K. A. Khor, P. Cheang, Effect of steam treatment during plasma spraying on the microstructure of hydroxyapatite splats and coatings, J. Therm. Spray Technol. 15 (2006) 610- 616.

[17] C. Popa, C. S. Ciobanu, S. L. Iconaru, M. Stan, A. Dinischiotu, C. C. Negrila, M. M. Heino, R. Guegan, D. Predoi, Systematic investigation and in vitro biocompatibility studies on mesoporous europium doped hydroxyapatite, Cent. Eur. J. Chem. 12 (2014).

[18] C. L. Popa, M. Albu, C. Bartha, A. Costescu, C. Luculescu, R. Trusca, S. Antohe, Structural characterization and optical properties of hydroxyapatite/collagen matrix, Rom. Rep. Phys. 68 (2016) 1149-1158.

[19] M. Kosec, B. Malic, A. Bencan, T. Rojas, KNN-based piezoelectric ceramics. In: A. Safari, E. Akdogan, Piezoelectric and acoustic materials for transducer applications, Springer Sci. Bus. Med. New York (2008) 81-102.

[20] J. Koruza, B. Malic, M. Kosec, Microstructure evolution during sintering of sodium niobate, J. Am. Ceram. Soc. 94 (2011) 4174-4178.

[21] P. Sumit, A. Avinash, K. Rai, Development of High Strength Hydroxyapatite for Hard Tissue Replacement, Trends Biomat. Arti. Organs 19 (2005) 46-51.

[22] J. Y. Rho, M. E. Roy, T. Y. Tsui, G. M. Pharr, Elastic properties of microstructural components of human bone tissue as measured by nanoindentation, J. Biomed. Mater. Res. 45 (1999) 48–54.

[23] P. K. Zysset, X. E. Guo, C. E. Hoffler, K. E. Moore, S. A. Goldstein, Elastic modulus and hardness of cortical and trabecular bone lamellae measured by nanoindentation in the human femur, J. Biomech. 32 (1999) 1005-1012

[24] D. T. Reilly, A. H. Burstein, The elastic and ultimate properties of compact bone tissue, J Biomech. 8 (1975) 393–396.

[25] E. F. Morgan, G. U. Unnikrisnan, A. I. Hussein, Bone Mechanical Properties in Healthy and Diseased States, Annu Rev Biomed Eng. 20 (2018) 119-143.

[26] A. K. Dubey, H. Yamada, K. Kakimoto, Space charge polarization induced augmented in vitro bioactivity of piezoelectric (Na,K) NbO_3, J. App. Phy. 114 (2013) 124701-124701.

[27] G. Shirane, R. Newnham, R. Pepinsky, Dielectric properties and phase transitions of $NaNbO_3$ and $(Na,K)NbO_3$, Phys. Rev. 96 (1954) 581.

[28] A. Saxena, K. Kakimoto, A. K. Dubey, Polarization induced dielectric and electrical response of electrovector hydroxyapatite and ferroelectric sodium potassium niobate ceramics, J. Phy. D: App. Phy. 53 (2020) 395402.

[29] W. Lingyan, R. Wei, M. Wenhui, L. Ming, S. Peng, Wu. Xiaoqing, Improved electrical properties for Mn-doped lead-free piezoelectric potassium sodium niobate ceramics, AIP Adv. 5 (2015) 097120.

[30] V. V. Atuchin, I. E. Kalabin, V.G. Kesler, N.V. Pervukhina, Nb 3d and O 1s core levels and chemical bonding in niobates, J. Electr. Spec. Rel. Phen. 142 (2005) 129-134.

[31] R. Shyam, D. Negi, P. Vashishtha, G. Gupta, A. Das, P. Dobbidi, S. R. Nelamarri, Study of light-emitting defects induced by 100 MeV Ag ion irradiation in potassium sodium niobate thin films, J. Lumin. 233 (2021) 117909.

[32] J. F. Moulder, W. F. Stickle, P. E. Sobol, K. D. Bomben, Handbook of X-ray photoelectron spectroscopy: A reference book of standard spectra for identification and interpretation of XPS data (Waltham, MA: Perkin-Elmer Corporation) 45 (1992).

[33] M. Wegmann, L. Watson, A. Hendry, XPS Analysis of Submicrometer Barium Titanate Powder, J. Am. Cer. Soc. 87 (2004) 371-377.

[34] X. Chen, L. Liu, P. Y. Yu, S. S. Mao, Increasing solar absorption for photocatalysis with black hydrogenated titanium dioxide nanocrystals, Science 331 (2011) 746-750.

[35] Y. Shuai, S. Zhou, D. Bürger, H. Reuther, I. Skorupa, V. John, M. Helm, H. Schmidt, Decisive role of oxygen vacancy in ferroelectric versus ferromagnetic Mn-doped BaTiO3 thin films, J. Appl. Phys. 109 (2011) 084105.

[36] W. Hu, Y. Liu, R. L. Withers, T. J. Frankcombe, L. Norén, A. Snashall, M. Kitchin, P. Smith, B. Gong, H. Chen, J. Schiemer, F. Brink, J. Wong-Leung, Electron-pinned defect-dipoles for high-performance colossal permittivity materials, Nat Mater. 12 (2013) 821-6.

[37] J. Hu, L. Wang, L. Shi, H. Huang, Preparation of $La_{1-x}Ca_xMnO_3$ perovskite–graphene composites as oxygen reduction reaction electrocatalyst in alkaline medium, J. Power Sour. 269 (2014) 144-151.

[38] C. C. Lin, C. C. Chen, C. M. Weng, S. Y. Chu, C. S. Hong, C.-C. Tsai, Effects of lithium doping on microstructure, electrical properties, and chemical bonds of sol-gel derived NKN thin films, J. Appl. Phys. 117 (2015) 085307.

[39] E. R. Moore, P. Ferrari, D. E. Diaz-Droguett, D. Lederman, J. T. Evans, Raman and X-ray photoelectron spectroscopy study of ferroelectric switching in $Pb(Nb,Zr,Ti)O_3$ thin films, J. App. Phy. 111 (2012) 14108.

[40] X. Li, Y. Wang, W. Liu, G. Jiang, C. Zhu, Study of oxygen vacancies′ influence on the lattice parameter in ZnO thin film, Mat. Let. 85 (2012) 25-28.

[41] L. Wan, W. Tian, N. Li, D. Chen, Q. Xu, H. Li, J. He, J. Lu, Hydrophilic porous PVDF membrane embedded with $BaTiO_3$ featuring controlled oxygen vacancies for piezocatalytic water cleaning, Nano Energy 94 (2022) 106930.

[42] R. Schaub, P. Thostrup, N. Lopez, E. Lægsgaard, I. Stensgaard, J. K. Nørskov, F. Besenbacher, Oxygen Vacancies as Active Sites for Water Dissociation on Rutile TiO_2 (110), Phys. Rev. Lett. 87 (2001) 266104.

[43] H. Hu, H. F. Ji, Y. Sun, The effect of oxygen vacancies on water wettability of a ZnO surface, Phys. Chem. Chem. Phys. 15 (2013) 16557-16565.

[44] H. Yu, J. Li, Y. Zhang, S. Yang, K. Han, F. Dong, T. Ma, H. Huang, Three-in-one oxygen vacancies: whole visible-spectrum absorption, efficient charge separation, and surface site activation for robust CO_2 photoreduction, Angew. Chem. Int. Ed. 58 (2019) 3880–3884.

[45] K. Das, S. Bose, A. Bandyopadhyay, Surface modifications and cell-materials interactions with anodized Ti, Acta Biomaterialia 3 (2007) 573–585.

[46] N. Yamada, T. Okano, H. Sakai, F. Karikusa, Y. Sawasaki, Y. Sakurai, Thermoresponsive polymeric surfaces – control of attachment and detachment of cultured-cells, Makromol Chem-Rapid 11 *(*1990) 571–576.

[47] B. A. Dikici, S. Dikici, O. Karaman, H. Oflaz, The effect of zinc oxide doping on mechanical and biological properties of 3D printed calcium sulfate based scaffolds, Biocyber. Biomed. Eng. 37 (2017) 733-741.

[48] A. K. Dubey, B. Basu, Pulsed Electrical Stimulation and Surface Charge Induced Cell Growth on Multistage Spark Plasma Sintered Hydroxyapatite-Barium Titanate Piezobiocomposite, J. Am. Ceram. Soc. 97 (2014) 481-489.

[49] K. Webb, V. Hlady, P. A. Tresco, Relative importance of surface wettability and charged functional groups on NIH 3T3 fibroblast attachment, spreading, and cytoskeletal organization, J. Biomed. Mater. Res. 41 (1998) 422–430.

[50] D. Khare, B. Basu, A. K. Dubey, Electrical stimulation and piezoelectric biomaterials for bone tissue engineering applications, Biomaterials 258 (2020) 120280.

[51] N. More, G. Kapusetti, Piezoelectric material - a promising approach for bone and cartilage regeneration, Med. Hypoth. 108 **(**2017) 10–16.

[52] J. Jacob, N. More, K. Kalia, G. Kapusetti, Piezoelectric smart biomaterials for bone and cartilage tissue engineering, Inflam. Regen. 38 (2018).

[53] M. Uo, M. Mizuno, Y. Kuboki, A. Makishima, F. Watari, Properties and cytotoxicity of water soluble Na_2O–CaO–P_2O_5 glasses, Biomaterials 19 (1998) 2277-2284.

[54] T. Arnett, Extracellular pH regulates bone cell function, J. Nutr. 138 (2008) 415S-418S.

[55] A. Galow, A. Rebl, D. Koczan, S. Bonk, W. Baumann, J. Gimsa, Increased osteoblast viability at alkaline pH *in vitro* provides a new perspective on bone regeneration, Biochem. Biophy. Rep. 10 (2017) 17-25.